ECAP-2016-018

Analysis of an excess flux of gamma rays at 30 degrees in longitude in the plane of the Milky Way galaxy

Bachelorarbeit aus der Physik

Vorgelegt von
Judith Höfer
22.08.2016

Erlangen Centre for Astroparticle Physics
Physikalisches Institut II
Friedrich-Alexander-Universität Erlangen-Nürnberg

Erster Gutachter: Prof. Dr. Stefan Funk
Zweite Gutachterin: Prof. Dr. Gisela Anton

Abstract

The *Fermi* space mission produced an all-sky map of the gamma ray sky. For testing our understanding of the processes emitting gamma rays models were constructed and residual count maps were derived from these. At 30° longitude in the Galactic plane an unexpected excess flux is seen.
In this work this residual flux is analysed in order to characterize it and make statements on how it is produced.
Therefore the spectra of the measured data and different residual maps averaged over a selected region of interest are derived. They are compared with all-sky spectra of different production processes and it is found that these all-sky spectra can not explain the data spectrum in the region of interest. This leads to the conclusion that there some yet unexplainable effects take place.
A multiwavelength analysis is started by studying data from the microwave telescopes *WMAP* and *Planck* and the infrared telescope *Spitzer* with particular observance of the region of interest. Excess flux also is seen in these other wavelength ranges. A first step in testing on correlations between these and the gamma ray excess is started by analysing if *WMAP* and *Fermi* data components could be effected by the same ultra-relativistic electrons. With the condition of a relatively high magnetic field in the region where the radiation originates a first requirement for this correlation is found.
Overall the existence of the excess at 30 degrees in longitude in the plane of the Milky Way galaxy is confirmed and a lot of possibilities for further investigations are found.

Contents

1 Introduction

The *Fermi* space mission produced an all-sky map of the gamma ray sky. This is seen in Figure 1. Right in the middle of the map lies the center of our Milky Way galaxy, the horizontal line of high excess is the Galactic plane. The high excess is due to a high density of cosmic rays and interstellar gas interacting and producing gamma rays there. Apart from that one can see point sources distributed over the sky.

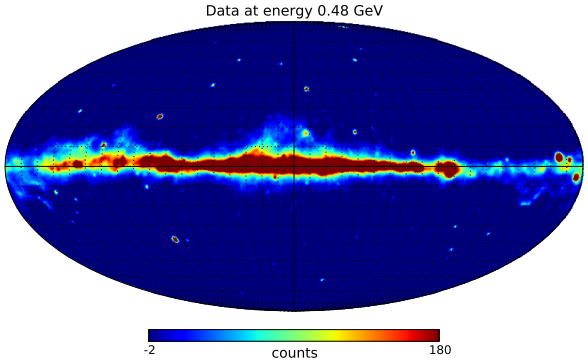

Figure 1: All-sky map of *Fermi* LAT data at an energy of 0.48 GeV

For testing our understanding of the processes emitting gamma rays in the galaxy models were constructed and compared to the observation. To test these models residual maps, i.e., maps showing the residual counts after subtracting the predicted model counts from the measured counts are made, one can be seen in Figure 2.

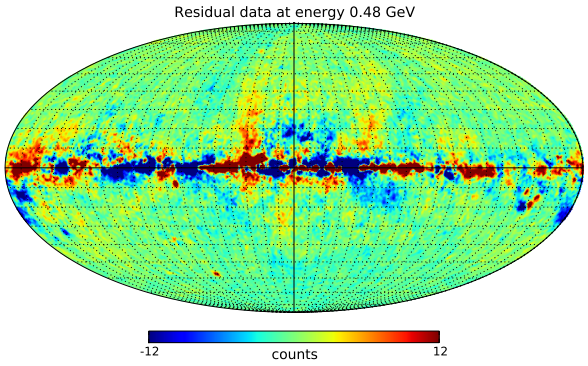

Figure 2: All-sky map of residual data at an energy of 0.48 GeV

Even though these models are very accurate by now there are some regions in the sky where they can not explain the measurement. One of these is a diffuse region at 30° longitude (left beside the Galactic center) at hight of the Galactic plane.

The following work will analyse this diffuse region in order to characterize the excess and make statements about the possible sources.

2 The gamma ray sky

2.1 Gamma astronomy

High energy astrophysics uses the upper 'end' of the electromagnetic spectrum to investigate the universe. The possibility to go to space opened this wavelength range to observations as gamma rays do not pass the atmosphere. Gamma rays are photons with energies greater than ~ 100 keV ($\lambda \lesssim 0.01$ nm). At energies above 100 MeV the dominant processes emitting gamma rays are the decay of the π^0-meson, bremsstrahlung and the Inverse Compton scattering [Longair, 2011, p. 26]. Their relative contribution depends on the energy and the position on the sky.

2.1.1 *Fermi* and the *Fermi* LAT

The *Fermi* Gamma-ray Space Telescope[1] is a space mission launched on June 11, 2008 for studying the cosmos in gamma ray range from 10 keV to 300 GeV (or 20 MeV - 300 GeV for the LAT instrument, respectively). One of its mission goals was the generation of an all-sky map.

The first gamma rays were detected by the *OSO III* satellite in 1967. Following satellite missions improved our knowledge of the gamma ray universe further and further: there is a diffuse gamma ray background mostly from outside our Galaxy (first detected by *SAS-2*) and also there are discrete gamma ray sources (e.g., pulsars in supernova remnants, first seen by *COS-B*). The first all-sky map was recorded by the *Energetic Gamma Ray Experiment Telescope* (*EGRET*) instrument of the Compton Gamma-Ray Observatory [Longair, 2011, p. 26].
In Figure 3 one can see all-sky maps from *SAS-2*, *COS-B*, *EGRET* and *Fermi* LAT. Interesting are the total count values.

The Large Area Telescope (LAT) is the main instrument onboard *Fermi*. It is - compared to the former EGRET - very sensitive and has a large field of view.
Some of its technical data is shown in Table 1.

energy range	20 MeV - 300 GeV
field of view	> 2 sr
angular resolution	$< 3.5°$ (100 MeV)
(for a single photon, 68% containment, on-axis)	$< 0.15°$ (>10 GeV)
energy resolution	< 10 %

Table 1: Technical data of the LAT onboard the *Fermi* Gamma-ray Space Telescope [NASA, 2011]

The measurement of the gamma rays works by detection of produced e^+ e^- - pairs. Incoming gamma rays first pass an anticoincidence shield sensitive to charged particles, then enter conversion foils. These contain very heavy nuclei which prompt the photons to decay into an electron and a positron. These go on through a particle tracing detector measuring the trajectories and a calorimeter measuring the energies.
Combining the different information, a gamma ray has a significant signature: (1) no signal in

[1] http://fermi.gsfc.nasa.gov/science/overview.html

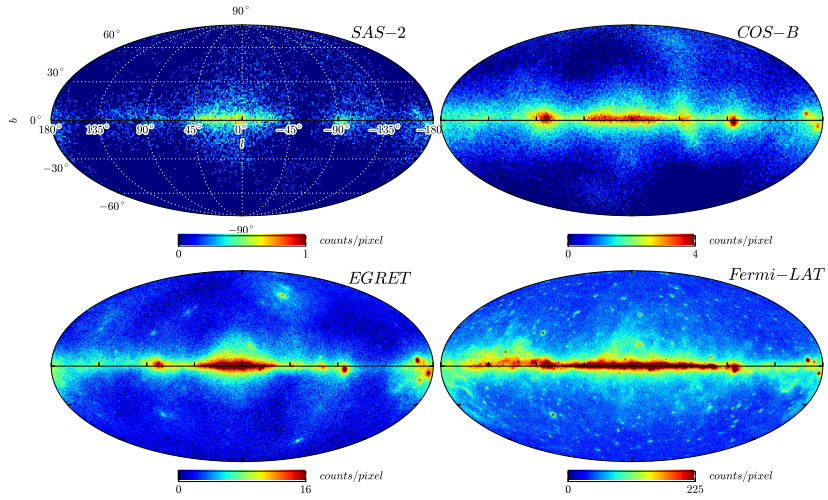

Figure 3: Mollweide projections in Galactic coordinates of accumulated counts maps for SAS-2, COS-B, EGRET (above 50 MeV) and *Fermi* LAT (above 360 MeV, 4 years, Clean class events). Regions with enhanced numbers of counts due to a non-uniform exposure time in observations with pointed observations are apparent in panels corresponding to *SAS-2*, *COS-B*, and *EGRET* [Acero et al., 2016, Figure 1 there].

the anticoicidence shield, (2) more than one e^+ or e^- track starting in the detector, and (3) a electromagnetic shower in the calorimeter [NASA, 2011].
The second instrument onboard the *Fermi* satellite is the Gamma-ray Burst Monitor. It has a field of view larger than the LATs and is constructed to detect gamma ray bursts.
In the following '*Fermi*' will call the *Fermi* LAT.

2.1.2 Contributions to the gamma ray sky

Figure 4 shows an all-sky map of the gamma ray sky at an energy of 1.37 GeV. The total flux can be separated into different contribution parts:

- *individually detected sources, point sources*
  Some objects (e.g. pulsars) emit gamma rays themselves.

- *diffuse emission due to interaction of cosmic rays with gas and radiation fields*
  Cosmic rays propagating through the Galaxy interact with interstellar gas and the interstellar radiation field. The resulting flux of gamma rays as end product depends on the density distribution of cosmic rays, the interstellar gas and the interstellar radiation field. The emitting processes themselves are described in section 2.2.3 (interstellar gas) and 2.2.4 (interstellar radiation fields).
  Part of this diffuse emission is the so-called Loop I, a - from our point of view - huge feature on the sky. Concerning this also see section 2.3.

- *isotropic diffuse gamma ray background*
  The isotropic diffuse gamma ray background contains diffuse extragalactic emissions and any Galactic foreground emissions that are approximately isotropic.

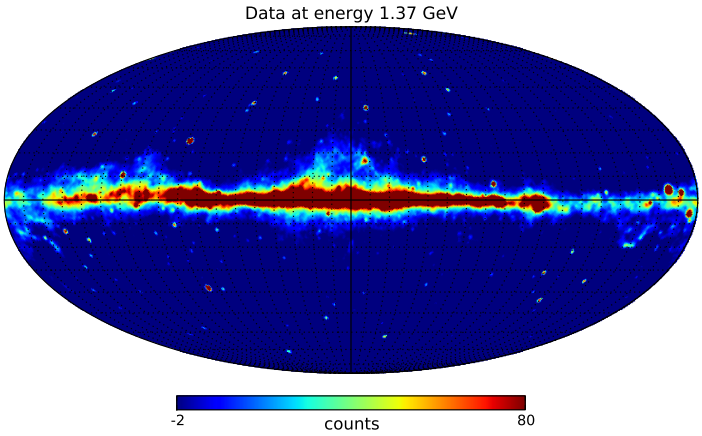

Figure 4: All-sky map of the gamma ray sky at an energy of 1.37 GeV. The map is smoothed with a $\sigma = 0.5°$ Gaussian kernel, the grid is 10° by 10° in Galactic coordinates.

2.2 Sources of gamma radiation

2.2.1 Point sources

Many individual sources emit gamma rays, e.g., pulsars, supernova remnants or quasars. Further away the Galactic plane mostly active galactic nuclei are seen as point sources [Longair, 2011, p. 26].

2.2.2 Cosmic Rays

Cosmic Rays (CRs) are protons, electrons or nuclei travelling through space. Approximately 85% of the CRs are protons, 12% are helium nuclei, 2% are electrons and 1% are heavier nuclei. The energies of CRs cover a very large range from 10^8 to 10^{20} eV and more [Longair, 2011, p. 493]. For energies between 10^9 and 10^{14} eV the spectrum can be described by $N(E)dE = kE^{-x}dE$ with $x \approx 2.5 - 2.7$.

Where these CRs come from is not yet well explored. Possible sources are, e.g., supernovae accelerating particles up to these very high energies, but not all effects are explained until now [Longair, 2011, pp. 30].

The CRs propagating through the Galaxy interact with the Interstellar Gas (ISG), e.g., they collide with the gas and with the Interstellar Radiation Field (ISRF), this is called Inverse Compton effect. Gamma rays are produced in these interactions.

2.2.3 Interstellar Gas

Interstellar Gas (ISG) is part of the interstellar medium, it provides ~ 5% of the visible mass in our Galaxy [Longair, 2011, p. 333]. The ISG contains lighter elements being in gas phase, mostly neutral hydrogen (H_I), ionized hydrogen (H_{II}) and molecular hydrogen (H_2) as well as helium (He). The interstellar medium also includes atoms or molecules in other phases (and CRs). Heavier elements mostly occur as dust grains. Dust is present nearly everywhere (as long as the temperature is not higher than the materials sublimation temperature), but it provides only ~ 1% of the interstellar medium [Herbst, 1995].

There are two types of interactions that can produce gamma rays from CRs meeting ISG: the decay of the π^0 meson and bremsstrahlung.

π^0 decay

CRs contain mostly protons and also some heavy nuclei. They can collide with the ISG, this is referred to as the *hadronic component* of gamma emission since protons are hadrons. In these collisions pions, π^-, π^+ and π^0, are produced. The charged pions decay into muons (antimuons) and neutrinos, these again turn into electrons (positrons) with relativistic energies and neutrinos. The π^0 on the other hand decays mostly (BR $\approx 99\,\%$) into two photons.

$$\mathrm{p} + \mathrm{H} \rightarrow \pi^0 + \mathrm{ANYTHING}$$
$$\pi^0 \rightarrow \gamma + \gamma$$

It has a mass of $\sim 135\,\mathrm{MeV}$ and is rather short lived, the mean lifetime is $\sim 9 \cdot 10^{-17}$ s. The spectrum of the outgoing gamma rays indicates the π^0 decay process. The maximum is broad and in the center of mass system of the π^0 centered about 70 MeV [Longair, 2011, pp. 503].

bremsstrahlung

Also the CR electrons can interact with the ISG. This process is often referred to as the *leptonic component* of gamma emission since electrons are leptons. When fast electrons - as they are part of CRs - feel the Coulomb field of a charged particle - as it is found in the ISM - they can emit a photon and slow down due to this emission. The process is called bremsstrahlung, the energies of the emitted photons are located in the gamma regime for interstellar processes [Rybicki and Lightman, 2004, p. 155].

Since both processes - π^0 decay and bremsstrahlung - are dependent on the distribution of CRs and the ISG in space they are often combined into one template during the derivation of models for the gamma ray emission.

2.2.4 Interstellar Radiation Field

The Interstellar Radiation Field (ISRF) is the radiation or the interstellar photon population, respectively, found in space. In Figure 5 the energy density of the ISRF is shown. One can see three maxima. The first one lies in the microwave frequencies, referred to as the Cosmic Microwave Background (CMB). The energy of the peak lies around $1 \cdot 10^{-3}\,\mathrm{eV}$. The second peak lies in the Infrared (IR) frequencies and has an energy about $1 \cdot 10^{-2}\,\mathrm{eV}$. The third one lies in optical frequencies, it is referred to as Starlight (SL), and it has an energy about $1\,\mathrm{eV}$. The maximum of the SL is around five times bigger than the one of the IR, the CMB background is independent on the spatial position.

The effect by which CRs interacting with the ISRF can produce gamma rays is called Inverse Compton effect.

Compton scattering was first observed in 1923 when A. Compton scattered hard X-ray radiation on stationary electrons. He saw an energy-loss (a greater wavelength) of the X-rays, the explanation was an energy and momentum transfer from the light to the electron.

Inverse Compton scattering now is not a down-scattering of the photon but an up-scattering through ultra-relativistic electrons. The energy of the electron is transferred to the ISRF

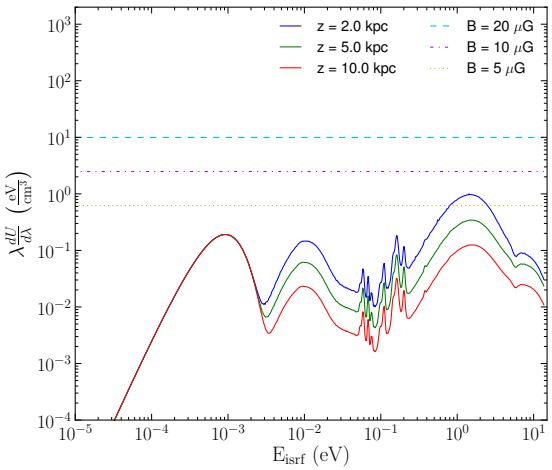

Figure 5: Energy density of the ISRF (including CMB) at different heights above the Galactic center z = 2, 5, 10 kpc. The horizontal lines are the energy density of 5, 10, and 20 μG magnetic fields [Ackermann et al., 2014, Figure 42 a) there].

which then has much more energy, the spectrum of the process goes up to gamma energies [Longair, 2011, p. 231].
One can approximate the energies of the via IC produced gamma rays by upscattering photons with energies at the maximum of the ISRF distribution. These give - simply due to their high quantity - the main distribution to gamma ray emission from IC.
Some details of the IC effect are also discussed in section 5.3.2.

The above mentioned processes have different typical spectra. These are shown in Figure 6. The π^0 spectrum peaks around 1 GeV, the bremsstrahlung spectrum peaks at lower energies of about 200 MeV. The π^0 peak is at higher energies than the 70 MeV peak in the center of mass frame because the π^0 is boosted in the laboratory frame. The IC spectrum also peaks at lower energies and is even broader.

2.2.5 Isotropic background

The Isotropic Diffuse Gamma Ray Background (IGRB) is a residual all-sky emission comprising all extragalactic emission too faint or too diffuse to be resolved, as well as any residual Galactic foregrounds that are approximately isotropic. The IGRB spectrum can be described over nearly four decades by a power law having a spectral index of ~2.3 with a cut-off energy of ~300 GeV [Ackermann et al., 2015b].

2.3 Loop I and the North Polar Spur

Loop I is a bright and - from our point of view - huge circular feature on the sky. It is seen in radio and X-ray frequencies as well as in gamma energies.
Its shape can be seen in the residual data shown in Figure 7. The Loop 'starts' at ~ 30° longitude in the Galactic plane, goes up to nearly the pole above the Galactic center and then again down

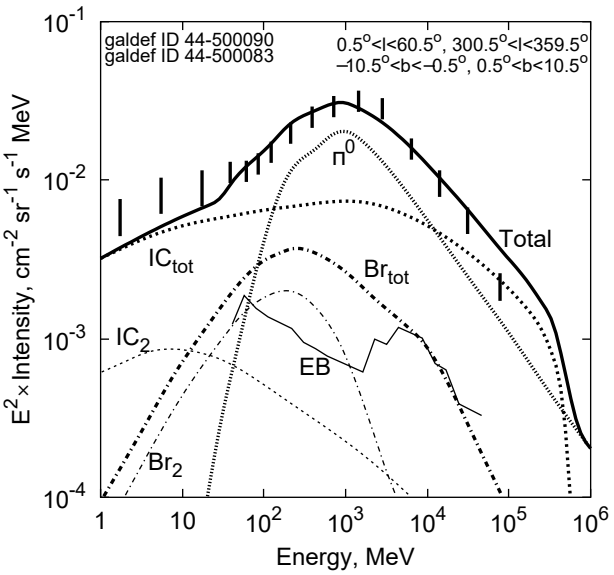

Figure 6: Spectra of the processes emitting gamma rays. They are derived by models also containing secondaries, i.e., particles which are just produced in the shown interaction and now can take part in it again. The spectra are shown with primary electrons (thick lines) and without (thin lines). Br_{tot} and Br_2 denote the total bremsstrahlung and the separate contribution from secondary leptons, correspondingly. Similarly, IC_{tot}, IC_2 indicate the total IC and the contribution from secondaries [Strong et al., 2004, Figure 13 there].

at the 'right' side of the center.

In radio frequencies more such features, e.g., one having the solar system inside called the 'Local Loop' are seen, they are called radio loops. The North Polar Spur (NPS) is a 'filament' inside this Loop I and seen mostly in radio frequencies. It possibly originates from the compression of gas by a supernova remnant or some other shock. Until now it is not sure how far Loop I is away and where it comes from.

Earlier it "has been concluded by several authors (e.g. Berkhuijsen et al. 1971; Heiles 1979; Salter 1983, and references therein) that the radio loops are correlated with expanding gas and dust shells, energized by supernovae or stellar winds." [Wolleben, 2007]

Wolleben [Wolleben, 2007] reproduced the shape of the Loop I and the Local Loop, there called the 'New Loop', with a geometric model. It is made of two shells characterized mainly by a position and an inner and an outer radius. The solar system lies between the inner and the outer surface of the Local Loop shell. The characteristics of the shells will also be described further in section 3.2. This geometric model could give a hint on where these loops come from. It tends to say that both loops are products of supernovae, that have taken place in the SCO-CEN OB association (Scorpius–Centaurus Association, a region of recent massive star formation [Preibisch and Mamajek, 2008]). Also it tends to say the Local Loop is older than Loop I and both just have started to interact, building the NPS there. But this scenario is not proven yet.

Later Kataoka et al. [Kataoka et al., 2013] analyzed X-ray data measured by *Suzaku* and saw that an interpretation in which the X-rays have travelled a long distance through gas from their origin is likely. Their conclusion was that it is preferred for Loop I being far away and being related to previous activity within/around the Galactic center and less preferred for it

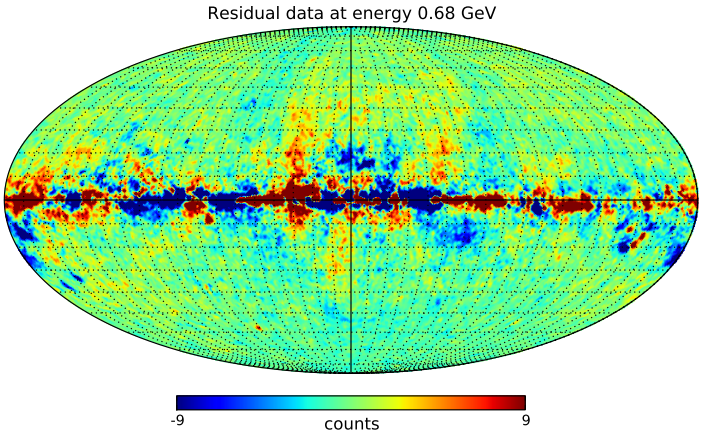

Figure 7: All-sky residual map of the gamma ray sky at an energy of 0.68 GeV. One can see Loop I above the Galactic plane. The map is smoothed with a σ = 0.5° Gaussian kernel, the grid is 10° by 10° in Galactic coordinates.

being near - but the possibility for it being a near feature is not eliminated.

The fact that the yet unexplained Loop I 'starts' at ~ 30° longitude in the Galactic plane combined with the unexpected excess flux seen by *Fermi* in this region motivates the following analysis.

3 Data sample

3.1 Total data map

The *Fermi* Science Support Center[2] provides several data products, organized in different classes selected for different uses.
For this analysis the Pass 8 UltraCleanVeto data sample class is used. This class provides the highest purity against contamination from charged particles that were misclassified as gamma rays. Some characteristics of the data sample are listed in Table 2.

class	P8 UltraCleanVeto
observation time	6.5 years recorded between August 4, 2008 and January 31, 2015 using standard good-time intervals (e.g. no calibration runs)
zenith angle cut	$\theta < 90°$
energy bins	31 equal logarithmic intervals
energy range	~28 MeV - ~1.4 TeV
HEALPix[3] pixelization order	7
HEALPix nside value	128
pixel size	~$6.4 \cdot 10^{-5}$ sr

Table 2: Characteristics of the used data sample

For a diffuse analysis - as it is done here - the purity of the signal is more important than the loss in statistics accompanied by the used hard cuts.

3.2 Residual data maps

Besides the total data map, different residual data maps are used. They were generated from models that were fitted to the total data maps. The residuals now are the remaining counts after the calculated model was subtracted from the total data. The different residual maps derived from the models named `A`, `B` and `C` differ in the used models, their fitting method and range and the energy bins.
In Figure 8 Mollweide projections of the three residual maps can be seen.

For the first map, the **residual in model `A`**, different components were fitted to the total data in 31 energy bins (the same bins as for the total data map described above). The map was derived by Dmitry Malyshev and Anna Franckowiak, a similar map was used in [Ackermann et al., 2014].
The first components were modelled from the CR populations predicted through GALPROP[4] and assumed gas distributions. GALPROP is a code calculating numerically the transport of CRs and the production of diffuse emission. It depends on various variables, some of these are shown in Table 8 (appendix), a more detailed description also can be found in [Ackermann et al., 2014, the GALPROP parameters there are the same, but the data selection is slightly different].

[2] http://fermi.gsfc.nasa.gov/ssc/
[3] http://sourceforge.net/projects/healpix/
[4] http://galprop.stanford.edu

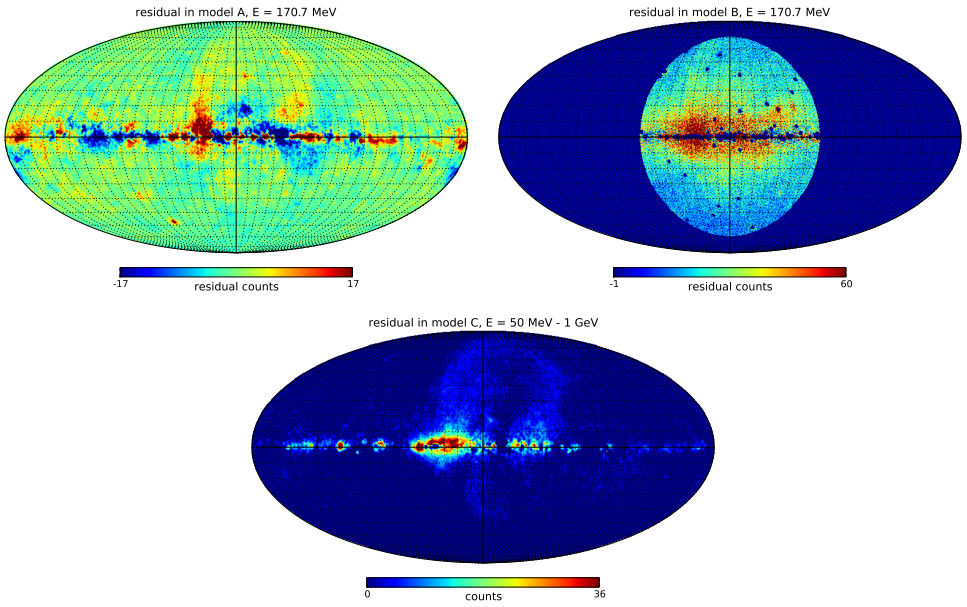

Figure 8: Mollweide projections of *top left:* residual in model `A` smoothed with a $\sigma = 0.5°$ Gaussian kernel, *top right:* residual in model `B` and *bottom:* residual in model `C` smoothed with a $\sigma = 0.5°$ Gaussian kernel. The grid is 10° by 10° in Galactic coordinates.

Beside the CR distribution also a distribution of target gas is needed. This is based on multiwavelength surveys. The densities of the gas are based on the 21-cm line of H_I [Kalberla et al., 2005, LAB survey] and the 2.6-mm line of CO [Dame et al., 2001]. H_2 is traced by this CO. There is also dark neutral gas not traced by H_I or CO this was taken into account by the dust reddening map of Schlegel et al. [Schlegel et al., 1998].

The templates for the emission from interstellar gas are parted into five Galactrocentric annuli (three inner, one local and one outer), the borders are shown in Table 9 (appendix, [Ackermann et al., 2014] only used three rings: the inner annuli are combined into one).

Loop I (see section 2.3) is not represented in GALPROP. Here it was taken into account by a geometric model by [Wolleben, 2007]. It assumes two shells emitting synchrotron radiation. Each shell has two coordinates of its center (longitude and latitude), a distance to the Galactic center and an inner and an outer radius. The values of the parameters are shown in Table 10 (appendix). The so-called *Fermi* bubbles are also a large scaled emission component. They are seen in gamma rays as two lobes above and below the Galactic center. They were modelled by a flat intensic spatial at $|b| > 10°$ (see Figure 28, appendix).

The point sources were implemented from the third *Fermi* LAT source catalog (3FGL, [Acero et al., 2015]). Of the extended sources the Large Magellanic cloud (a nearby galaxy seen in gamma rays due to massive star-formation [Ackermann et al., 2015a]) and the Cygnus region (a region filled with numerous massive stellar clusters and a large CR density [Tibaldo and Grenier, 2013]) got its own template each.

Also a Galactic center excess (GC excess) template was included to take into account the effects that occur near the Galactic center and are not yet explored. In some theories this could be annihilation of dark matter particles. The GC excess template describes annihilation that follows a generalized Navarro-Frenk-White profile with index $\gamma = 1.25$ and that is brightest around the

Galactic center.
So the different components of the model are:

- five pairs of hadronic correlated components for the emission from the five annuli of interstellar gas, each containing one template for H_I and one template for CO interacting with CRs. The bremsstrahlung components were fitted together in one template with these hadronic components.
- three IC components from upscattered CMB, IR and SL (therefore also see section 2.2.4)
- a template for Loop I
- a template for the *Fermi* bubbles
- a template for point sources in each energy bin
- a template for the Large Magellanic cloud and the Cygnus region each
- a template for other extended sources
- a GC excess template
- a sun and moon template (they also emit gamma rays) derived with the *Fermi* ScienceTools
- an isotropic component, which is constant over the whole sky

The templates for the hadronic, the IC, the *Fermi* bubbles and the geometric Loop I model can be seen in Figure 28 (appendix).
There was no template for the Earth limb, i.e., the gamma rays produced due to CRs interacting with the earths atmosphere also seen by *Fermi* since it is not yet constructed for the Pass 8 data. Therefore the zenith angle was cut to $< 90°$ (see Table 2 above).
The fitting procedure uses the χ^2 method to fit the all-sky templates to the all-sky data in each of the 31 energy bins. A similar method is used here later on (detaild description in section 4.4), but here later on a model spectrum is fitted to a mean spectrum of measured data in a certain region.
The models for the second map, the **residual in model `B`**, were produced by the same procedure as the ones for the residual in model `A`, but the templates were slightly modified (see description below). Also the area in which the templates were fitted to the total data was restricted and less components were taken into account.
The fitting area was restricted to a circle with radius 70° around the Galactic center instead of the whole sky and only the following modified templates were included:

- the hadronic correlated templates were modified to three annuli: the formerly inner rings were combined into one ring (radii 0 - 8 kpc), beside this the same local and outer rings were used. There is a H_I and CO template including bremsstrahlung for each ring
- the three IC templates were also combined into one
- the point sources and the extended sources templates are as before

– the isotropic component, the Loop I and the *Fermi* bubbles templates were replaced by a combination of 100 spherical harmonics. These also model other possible components.

The residual map was calculated by subtracting the mentioned model maps except the spherical harmonics from the total data map. Hence for deriving the spectrum of the residual in model `B` also an isotropic component is subtracted.
The third map, the **residual in model `C`**, was derived by ACERO ET AL. [Acero et al., 2016]. It has three energy bins: 50 MeV - 1 GeV, 1 - 11 GeV and 11 - 50 GeV. The characteristics of the underlying total data map are slightly different than the ones of the map used for the residuals in model `A` and `B`, they are listed in Table 11 (appendix).
The residual - it includes more diffuse emission components than the residual in model `A`, e.g., Loop I or the *Fermi* bubbles and is called Extended Excess Emission (EEE) - was derived by subtracting the following model components from the total data:

– a hadronic correlated emission component, also separated into different Galactocentric annuli

– an IC component

– a template for the point-like and small-extended sources from the preliminary version of the 3FGL catalogue

– a Earth limb template for the gamma rays produced due to CRs interacting with the earths atmosphere

– a sun and moon template

– an isotropic component

ACERO ET AL. refer to this combination as the 'baseline' model, for more details see their description [Acero et al., 2016].
The fit used a binned maximum likelihood with Poisson statistics and included the whole sky. Since the residual map only contains three energy bins it is not used to derive spectra, but a profile plot is studied in section 5.2.

3.3 Exposure map

The exposure map encodes the exposure time and the effective area of the LAT during the mission for every pixel on the sky. It was calculated using the standard *Fermi* LAT ScienceTools package version 10-01-01 available from the *Fermi* Science Support Center using the P8R2_ULTRACLEANVETO_V6 instrument response functions[5].

[5] http://fermi.gsfc.nasa.gov/ssc/data/analysis/

4 Analysis of the spectrum

4.1 Selection of the region of interest

For this analysis the Region Of Interest (ROI) is selected by eye. It is located in the excess region but is restricted not to include too much of the Galactic plane.
In Figure 9 one can see the residual in model `A` and a map showing the position and shape of the RIO. In Table 3 the exact borders are shown.

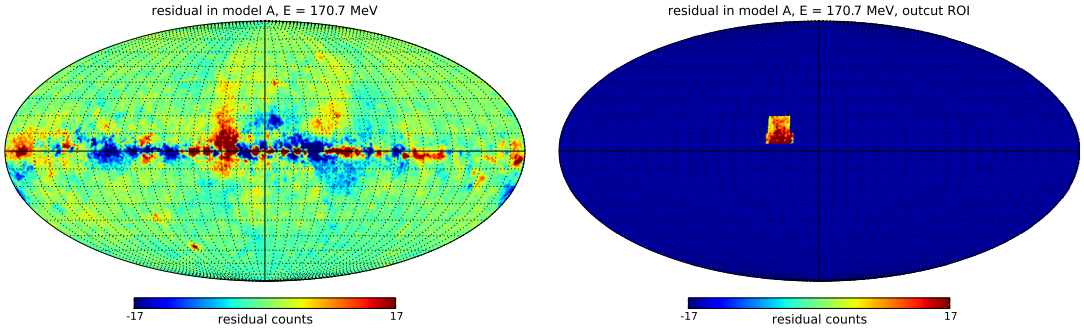

Figure 9: *left:* residual in model `A`, *right:* residual in model `A` showing the position and shape of the RIO.
Both maps are smoothed with a $\sigma = 0.5°$ Gaussian kernel, the grid is 10° by 10° in Galactic coordinates.

	longitude: lower end	longitude: upper end	latitude: lower end	latitude: upper end
	18°	37°	4°	10°
combined with	21°	36°	10°	20°

Table 3: Borders of the region of interest

4.2 Spectrum

All maps shown up to this point are photon count maps. For the spectra the intensity I per pixel per energy bin is calculated from these count maps. It is defined as

$$I = E\frac{dI}{dE} = E^2\,\frac{dN}{dE} = E^2\,\frac{counts}{exposure\;\Delta E\,\mathrm{d}\Omega}$$

in every energy bin from $E_{\text{lower end}}$ to $E_{\text{upper end}}$.
$\frac{dN}{dE}$ is the photon flux[6], *counts* the count value in this pixel in this energy bin, *exposure* the exposure value in this pixel in this energy bin, ΔE the size of the energy bin and $\mathrm{d}\Omega$ the pixel size.
The maps used here are pixeled in HEALPix (Hierarchical Equal Area isoLatitude Pixelization of a sphere)[7]. As the name suggests this has the advantage of every pixel having the the same size. So $\mathrm{d}\Omega$ is simply the whole sphere size of 4π in sr divided by the number of pixels. This is

[6] $\frac{dN}{dE}$ actually calls $\frac{dF}{dE} = \frac{dN}{dE\,dA\,dt}$, but the other notation is common
[7] http://healpix.jpl.nasa.gov/

depending on the HEALPix pixelization order. Here for example the order is 7, with this the number of pixels is 196,608 and therefore $\mathrm{d}\Omega \approx 6.4 \cdot 10^{-5}\mathrm{sr}$.
The energy bins are equal logarithmic, so:

$$E_{\text{lower end}} = \exp\Big(\ln(E) - \frac{\ln(\Delta E)}{2}\Big) = \frac{E}{\sqrt{\Delta E}} \quad \text{and} \quad E_{\text{upper end}} = \exp\Big(\ln(E) + \frac{\ln(\Delta E)}{2}\Big) = E \cdot \sqrt{\Delta E}$$

For the spectrum the average over the ROI is taken:

$$\begin{aligned}\langle I \rangle_{ROI} =& E^2 \, \langle \frac{dN}{dE} \rangle_{ROI} = E^2 \, \langle \frac{counts}{exposure} \rangle_{ROI} \, \frac{1}{\Delta E \, \mathrm{d}\Omega} \\ =& E^2 \, \Big(\frac{1}{n_{pix}} \sum_i \frac{counts_i}{exposure_i} \Big) \, \frac{1}{\Delta E \, \mathrm{d}\Omega}\end{aligned}$$

i.e., in each energy bin the average over all pixels i in the ROI of the counts and exposure per pixel is taken. E, ΔE and $\mathrm{d}\Omega$ are independent of the pixel.
For the residual maps the (mean) intensity is derived the same way:

$$\langle I_{res} \rangle_{ROI} = E^2 \, \langle \frac{dN}{dE}_{res} \rangle_{ROI} = E^2 \, \langle \frac{residual \ counts}{exposure} \rangle_{ROI} \, \frac{1}{\Delta E \, \mathrm{d}\Omega}$$

The calculation of the standard derivations assuming a Poisson statistics for the counts can be found in section A.6 (appendix).

In Figure 10 the spectrum of the total data averaged over the ROI is shown. On can see a peak around 0.5 GeV, at lower energies the values decrease slightly. At higher energies - in an energy range from ~ 2 GeV to ~ 1 TeV - one can see a power law distribution, i.e., the intensity is indirect proportional to the energy by the power of the spectral index s: $I \propto E^{-s}$.
Fitting a power law $I = const. \ E^2 \big(\frac{dN}{dE}\big)^{-s_n} = const. \ E^{-s_n+2}$ in this range (energy bins 13 - 30 were included)[8] gives a spectral index s of $s_n = 2.59$. The n as an index of the spectral index marks it as an index of the photon flux (and not of the intensity flux $\frac{dI}{dE}$). The fit is shown in Figure 29 (appendix).
The data point with the highest energy lies above the ones before, what could be the beginning of a turn-over. But this single point is not enough to state whether this is a real turn-over at higher energies or just fluctuations, even if the value is very high.
In Figure 11 the spectrum derived from the residual in model `A` is shown. One can see a peak around 0.1 GeV and the residual does not occur above 5 GeV.
Because the models for the residual in model `B` do not include an isotropic component, a spectrum for this is subtracted while calculating the residual map spectrum (see section 3.2). The used spectrum was derived by Ackermann et al. [Ackermann et al., 2015b], it is an all-sky spectrum of the isotropic background (see also section 4.3). Using this all-sky spectrum in the restricted ROI is not a problem, because the isotropic background is defined as being nearly the same over the whole sky. But it leads to the fact that the spectrum can only be calculated in 26 energy bins, because the isotropic background spectrum only was derived in these bins.

[8] The fit was derived by the χ^2 method due to fitting a straight $m \cdot \ln(E) + t$ to the logarithm of the data. This gives the same result because $\ln(I) = \ln(const. \ E^{-s_n+2}) = (-s_n + 2)\ln(E) + \ln(const.)$ and $s_n = -m + 2$.

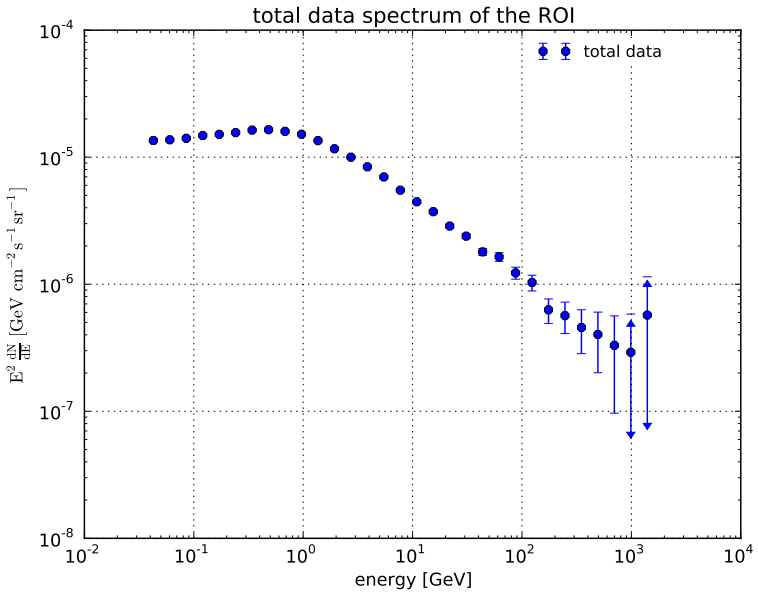

Figure 10: Spectrum of the total data averaged over the ROI.
It is shown as $E^2 \frac{dN}{dE}$ over E and both axis are logscale. For the last two data points the lower end of the errorbar is negative.

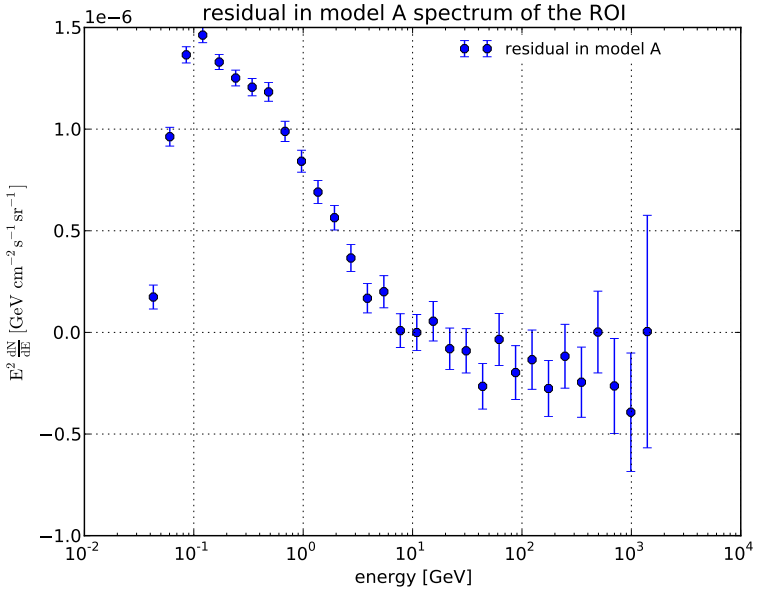

Figure 11: Spectrum of the residual in model `A` averaged over the ROI.
It is shown as $E^2 \frac{dN}{dE}$ over E and only the energy axis is logscale.

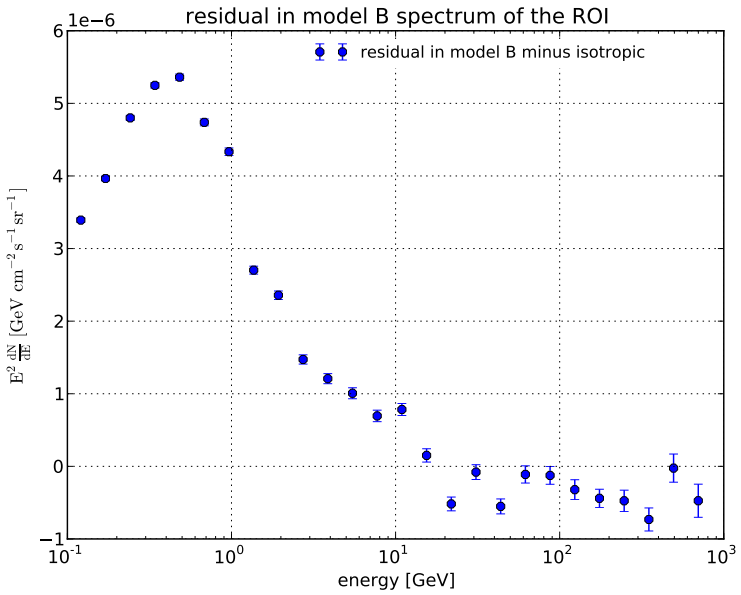

Figure 12: Spectrum of the residual in model `B` averaged over the ROI minus the isotropic spectrum [Ackermann et al., 2015b].
It is shown as $E^2 \frac{dN}{dE}$ over E and only the energy axis is logscale.

Figure 12 shows the spectrum derived from the residual in model `B`. The intensity values of the residual in model `B` are higher than the ones of the residual in model `A`. This is due to the fact that for `B` less models were taken into account and subtracted from the measured data.
The spectrum of the residual in model `B` differs from the spectrum derived from the residual in model `A` (different models are used), but one also can see a maximum below 20 GeV and no residual above. The peak here is about 0.4 GeV.
This clearly shows that there is an unexpected excess flux of gamma rays with energies about 0.03 GeV (or even less and then not seen by *Fermi*) to 10 GeV.
The residual in model `C` has - as mentioned - only three energy bins, so a spectrum will not be derived.

4.3 All-sky models

Ackermann et al. [Ackermann et al., 2015b] analysed the spectrum of the Isotropic Diffuse Gamma Ray Background (IGRB). For this analysis they modelled different diffuse emission components and determined their all-sky spectra. The characteristics of their data sample are shown in Table 12 (appendix). They used the P7 UltraClean class but modified it (different for two energy ranges: 100 MeV - 13 GeV and 13 GeV - 820 GeV) to even harder cuts against misclassified CRs, for more details - also about the following models - see their description.
The model components are:

- two templates for the diffuse Galactic emission due to CR interaction with ISG (named '$H_I + H_{II}$', here it is named 'Gas' for a clearer spelling.) and ISRF (named 'IC')
- one template for local diffuse emission from Loop I and the Local Loop

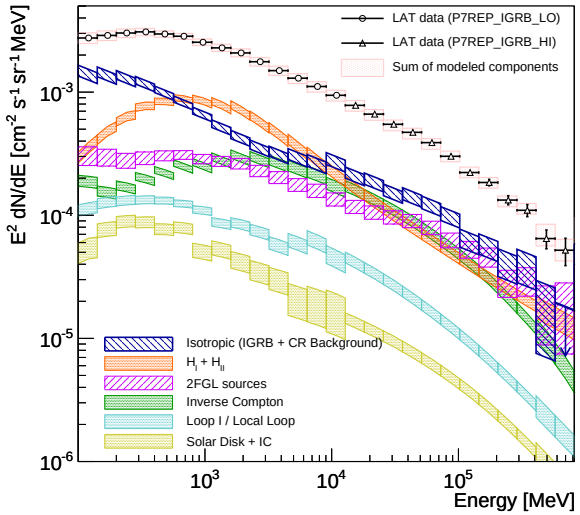

Figure 13: Fitted average intensity of the diffuse Galactic emission in foreground model A for Galactic latitudes $|b| > 20°$ derived by Ackermann et al. [Ackermann et al., 2015b, Figure 4 there].

- 403 templates for point sources, that are fitted individually
- one template for other point sources
- one template for the solar disc and the IC associated with the solar radiation field
- one template for the IGRB

The templates for the diffuse Galactic emission were derived using the GALPROP code. Loop I was modelled by the geometric model [Wolleben, 2007] also used for the model `A` (see section 3.2 and Figure 28, appendix). The point sources are from the 2FGL catalog.
The fit was made by a multi-component maximum likelihood method. In the lower energy range all templates were fit individually in each energy bin over the whole sky (excluding the mask, see below). In the higher energy range the IGRB and the single point source templates were fitted in each energy bin, but the other templates were fitted in all the higher energy bins together (i.e., the normalization is the same for each bin).
During the fit a mask covering mostly the Galactic plane was used, regions under the mask were excluded from the fit. Figure 30 (appendix) shows an all-sky map and the overlaid mask.
Here Ackermann et al.s so-called model A is used. (Model B and C assume other values for the GALPROP parameters and therefore derive slightly different Gas correlated and IC templates.)
Figure 13 shows the total all-sky spectrum and the models' spectra they derived. It displays the average high-latitude ($|b| > 20°$) intensities attributed to the isotropic emission (IGRB plus CR background), the individual sources, two diffuse Galactic emission components, the solar emission, and the local foreground templates. The sum of these intensities is compared to the average gamma ray intensity observed by *Fermi*.
Here a linear combination of some of these model components' spectra is fitted to the data spectrum of the ROI. This can provide information about how the gamma ray emission is composed.

4.4 Fitting procedure

For fitting the χ^2-minimization method was used. χ^2 is

$$\chi^2 = \sum_i \frac{(d_i - \mu_i)^2}{\sigma_i^2}$$

where d_i is the measured intensity and σ_i the standard derivation in energy bin i. μ_i is the linear combination of the different model components m_k in energy bin i: $\mu_i = \sum_k f_k m_{ki}$.
The coefficients f_k encode how much the model component m_k contributes to the whole model μ. They are the changed variables during the minimization of χ^2.

$$\frac{\partial \chi^2}{\partial f_k} = 0$$

χ^2 is quadratic in f_k, so the minimization is a system of linear equations in f_m and therefore - provided the model components are independent, what we assume here - has a unique solution.

4.5 Comparison of the ROI spectrum with all-sky spectra

Because the all-sky spectra by Ackermann et al. [Ackermann et al., 2015b] were only derived in 26 energy bins, the following analysis will be restricted to this range.
In Figure 14 the spectrum of the ROI and the Gas correlated and IC model spectra are shown, from the total data spectrum the isotropic spectrum [Ackermann et al., 2015b] was subtracted. The black data points are the sum μ of the Gas and IC spectra $\mu = f_{\text{Gas}} \cdot m_{\text{Gas}} + f_{\text{IC}} \cdot m_{\text{IC}}$ in each energy bin. Below the spectrum the relative difference $\frac{\mu - I}{I}$ between the intensity of the fitted model μ and the data intensity I is shown.
The spectrum of the model μ peaks around 0.7 GeV, at lower energies the values are below the data spectrum. At higher energies the values lie above the data spectrum and follow a power law. The spectral index is $s_n = 2.69$ an therefore nearly the same as the one for the total data spectrum (which was $s_n = 2.59$). The index was derived by fitting a power law with the same method as above (section 4.2). It can be seen in Figure 31 (appendix).
Even if the spectral indices are nearly the same and also the peaks are in the same range, the spectra show obvious differences and so the data spectrum can not altogether be explained through a linear combination of all-sky Gas correlated and IC spectra.
The absolute value of the normalization factor f does not have this much of meaning. More meaningful is the relation between the factors f_{Gas} and f_{IC}, which is 1:1 for the all-sky models. Here it is $f_{\text{Gas}} : f_{\text{IC}} = 16.5 : 11.6 \approx 1.4$. This - and also the plot - shows that the fit favours a Gas-to-IC relation higher than the one found over the whole sky.
In Figure 15 the spectra of the residuals in models `A` and `B` are compared with the all-sky spectra using the same method as above. The black data points are again the sum μ of the Gas and IC spectra $\mu = f_{\text{Gas}} \cdot m_{\text{Gas}} + f_{\text{IC}} \cdot m_{\text{IC}}$ in each energy bin. Here the model μ is not fitted in every energy bin, instead the fit is restricted to the energy range of the unexpected excess flux. The exact range can be seen at the model data points (and the dotted lines), they are restricted to the same range.

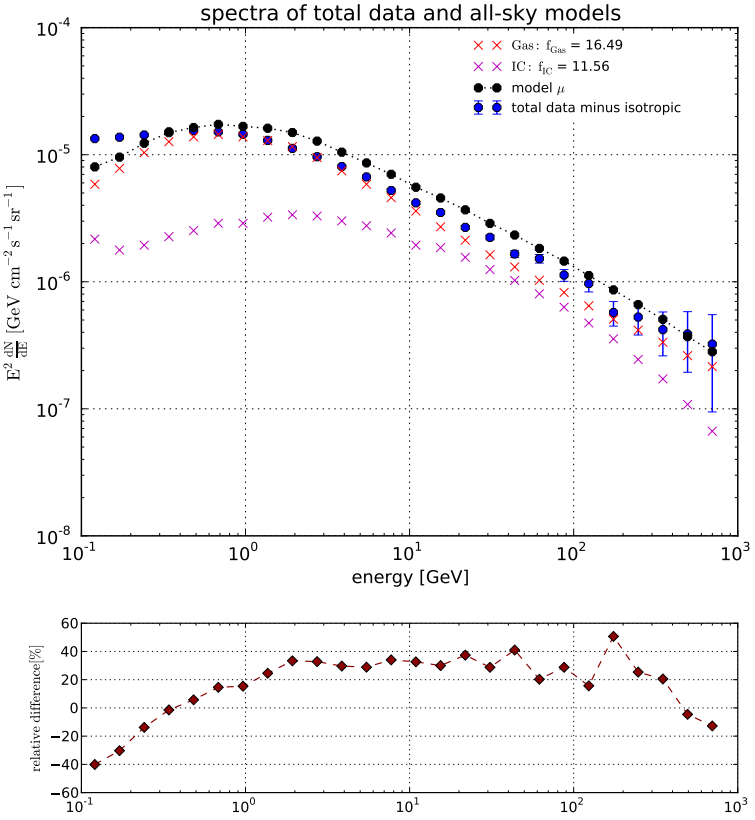

Figure 14: Spectrum of the total data map averaged over the ROI minus the isotropic spectrum, and the spectra of the Gas correlated and IC models [Ackermann et al., 2015b].
It is shown as $\mathrm{E}^2\frac{\mathrm{dN}}{\mathrm{dE}}$ over E and both axis are logscale. Below the relative difference is shown.

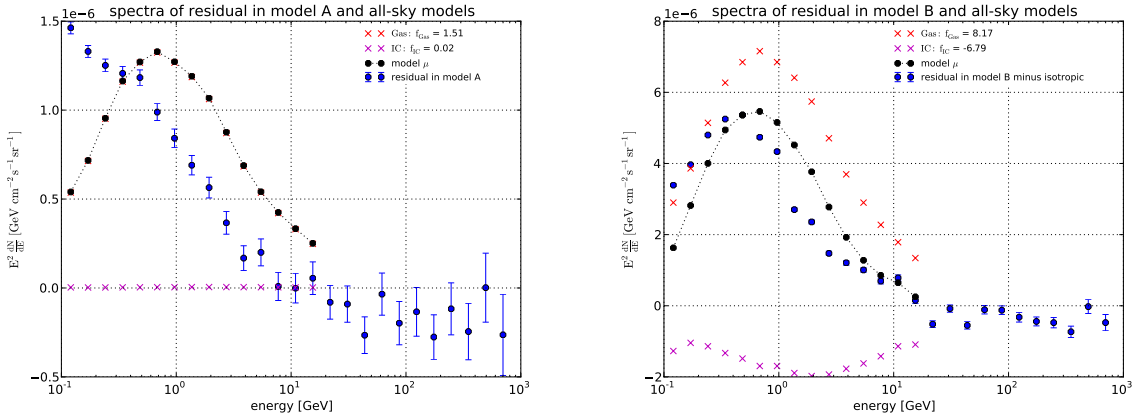

Figure 15: Spectra of the residual maps averaged over the ROI and the spectra of the Gas correlated and IC models [Ackermann et al., 2015b].
Left: residual in model `A`, *right:* residual in model `B` minus the isotropic spectrum.
It is shown as $\mathrm{E}^2\frac{\mathrm{dN}}{\mathrm{dE}}$ over E and only the energy axis is logscale.

The spectrum of the residual in model `B` is more accurately described by the model μ than the residual in model `A` because of the residual data peak being at higher energies, closer to the $\sim 0.7\,\mathrm{GeV}$ peak of the Gas correlated model.
For the residual in model `B` the IC spectrum is fit with a negative normalization factor. This is a hint for an over-estimation of the IC emission in the ROI by the model used to derive the residual. For the residual in model `A` f_{IC} is nearly zero.
The fit to the total data spectrum and to the residual data spectra together hint for a larger distribution of Gas emission in the ROI. But one has to be careful with further conclusions because the used model spectra are determined as spectra for the whole sky and are fitted to the data excluding the Galactic plane.

Also spectra from other templates were derived by Ackermann et al. [Ackermann et al., 2015b]. The fitted model spectra including also the Loop I / Local Loop and Point sources spectra next to the Gas correlated and IC are shown in Figures 16 (total data spectrum) and 17 (residual data spectra). The black data points are again the sum μ of the model components spectra $\mu = f_{\mathrm{Gas}} \cdot m_{\mathrm{Gas}} + f_{\mathrm{IC}} \cdot m_{\mathrm{IC}} + f_{\mathrm{LoopI}} \cdot m_{\mathrm{LoopI}} + f_{\mathrm{Point\ sources}} \cdot m_{\mathrm{Point\ source}}$ in each energy bin. For the total data map the relative difference $\frac{\mu - I}{I}$ between the intensity of the fitted model μ and the data intensity I is shown below the spectrum. For the residual data maps the fitting range for the model μ is again restricted to the energy range of the unexpected excess flux. The exact range can be seen at the model data points (and the dotted lines), they are restricted to the same range.
At lower energies (to about 6 GeV) the total data spectrum is well described by the spectrum of the model μ, but at higher energies the model overestimates the measured data.
The normalization factor of the IC spectrum is negative. The template for Loop I also contains emission from IC, but due to it being a geometric model one can not say how big the distribution is. If it was way smaller than the negative IC template distribution, the fit would be unphysical, because a in total negative IC emission is not possible. From the other components the point sources spectrum gives the highest distribution.
The residuals' spectra are relatively well described by the spectrum of the model μ. For both residuals the distribution from IC is fit with a negative normalization factor, so a lower distribution of IC is required. The fit to the spectrum of the residual in model `A` asks for a bigger distribution of point sources for its model. The distribution of Gas correlated and Loop I emission is said to be appropriate, the normalization factors are nearly zero. The fit to the spectrum of the residual in model `B` requires a bigger distribution from Gas and Loop I. For point sources it also asks for a bigger distribution, but not as big as the required one for the residual in model `A`. This is surprising because the same point sources template is used. It points out that one has to be careful with drawing further conclusions concerning the emission distribution in the ROI only from the normalization factors and the required distributions in the fit.
Nevertheless both the total and the residual data spectra give a hint for an underestimation of the point source density and again an overestimation of IC emission in the ROI.

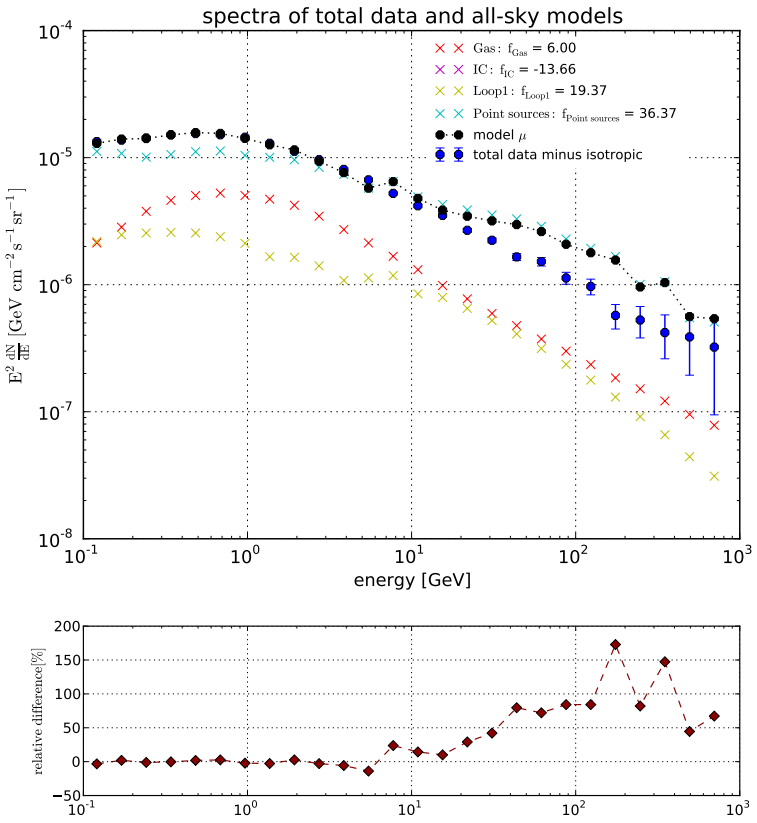

Figure 16: Spectrum of the total data map averaged over the ROI minus the isotropic spectrum, the spectra of the Gas correlated and IC and also Loop I / Local Loop and Point sources models [Ackermann et al., 2015b].
It is shown as $E^2 \frac{dN}{dE}$ over E and both axis are logscale. Below the relative difference is shown.

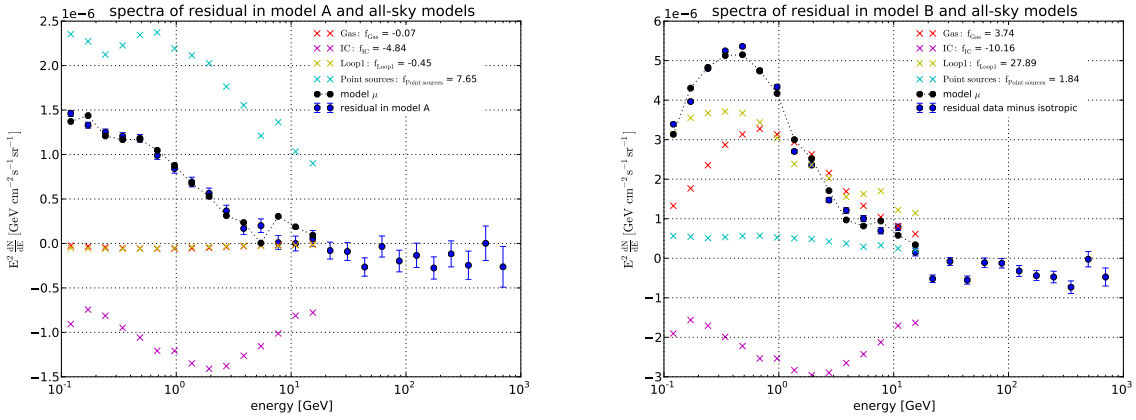

Figure 17: Spectra of the residual data maps averaged over the ROI, the spectra of the Gas correlated and IC and also Loop I / Local Loop and Point sources models [Ackermann et al., 2015b].
Left: residual in model `A`, *right:* residual in model `B` minus the isotropic spectrum.
It is shown as $E^2 \frac{dN}{dE}$ over E and only the energy axis is logscale.

Finally one can say that the made conclusions concerning distribution relations in the ROI are preliminary and that there is the need for further analysis of the spectra. Beside others there is the need, e.g., for a proper point sources template. Nevertheless one can state that there actually is an unexpected excess flux in the ROI and neither the total data nor the residual data can be explained by a linear combination of emission components averaged over the whole sky (all-sky spectra), i.e., there is something new going on.

5 Multiwavelength analysis

Photons emitted from processes in space do not only have energies in the gamma ray regime. Excesses seen in other frequencies - depending on their energy - also can support statements concerning the ongoing processes and therefore give a hint on the source of the gamma radiation.

5.1 Other telescopes

Here data from three other telescopes is used.

WMAP

The *Wilkinson Microwave Anisotropy Probe* (*WMAP*) telescope is a space telescope designed to detect microwave radiation. It was launched on June 30, 2001 to an orbit around the second Lagrange point of the earth-sun-system (Lissajous orbit about L2). The data sample used here are all-sky maps from the full nine years of spacecraft operations.

WMAP took data in five energy bands, named K, Ka, Q, V and W. Frequency and bandwidth are given in Table 4.

	K-Band	Ka-Band	Q-Band	V-Band	W-Band
wavelength	13 mm	9.1 mm	7.3 mm	4.9 mm	3.2 mm
frequency	23 GHz	33 GHz	41 GHz	61 GHz	94 GHz
bandwidth	5.5 GHz	7.0 GHz	8.3 GHz	14.0 GHz	20.5 GHz

Table 4: Wavelength, frequency and bandwidth of the WMAP-bands

The data exists as an all-sky map in the five mentioned energy bands. It is given in units of a brightness temperature T_b. This is defined via the black-body radiation: when the intensity of radiation from a region of sky is I_ν, the brightness temperature T_b is defined using the expression of the intensity of black-body radiation (Planck's law) [Longair, 2011, eq. A.36]:

$$I_\nu = \frac{2h\nu^3}{c^2} \frac{1}{e^{\frac{h\nu}{k_B T_b}} - 1}$$

In a range where $h\nu \ll k_B T_b$ holds (h is Planck's constant and k_B Boltzmann's constant), the Rayleigh-Jeans law is a good approximation to transform from the brightness temperature to the intensity of the radiation. It says [Longair, 2011, eq. A.37]:

$$I_\nu = \frac{2\nu^2 k_B T_b}{c^2}$$

where c is the speed of light. The requirement $h\nu \ll k_B T_b$ holds in the range we are looking at with *WMAP* data.

Planck

The *Planck* telescope is a space telescope also designed to detect microwave radiation. It was launched on May 14, 2009 to an orbit around the second Lagrange point of the earth-sun-system (Lissajous orbit about L2). The data sample used here are two of the diffuse foreground component maps derived from the *Planck* data by Adam et al. [Adam et al., 2015] with the help

of Commander[9]. Commander is an approach implementing Bayesian component separation in pixel space, fitting a parametric model to the data by sampling the posterior distribution for the model parameters[10]. Also data from *WMAP* and the 408 MHz survey by Haslam et al. [Haslam et al., 1982] was used to separate the foreground - beside others[11] - into synchrotron (see section 5.3.1), free-free (bremsstrahlung from non-relativistic particles, see also section 2.2.3), spinning dust (dipole radiation from spinning dust grains) and thermal dust (emission from dust grains in thermal equilibrium with the ambient radiation field [Abergel et al., 2014]) components. Here the synchrotron and the thermal dust foreground model maps are used.
The data also exists as all-sky maps and is given in units of a brightness temperature T_b. The requirement $h\nu \ll k_B T_b$ holds also in the range we are looking at with *Planck* data, so the Rayleigh-Jeans law was used to convert T_b into intensity.

Spitzer

The *Spitzer* telescope is a space telescope designed to detect infrared radiation. It was launched on August 25, 2003 to a heliocentric orbit and covers a wavelength range from 3 - 180 μm. The data sample used from *Spitzer* observations are from the GLIMPSE360 (Galactic Legacy Infrared Mid-Plane Survey Extraordinaire)[12] project. It shows the Galactic plane in infrared light as a collage from *Spitzer* and also other surveys.
The data is stored as an image file with RGB values and an alpha-channel (to encode transparency). The different color channels are filled with the intensities measured in different wavelength:

color channel	Red	Green	Blue
wavelength	8.0 μm	4.5 μm	3.6 μm

[13]Here the G channel, i.e., data measured at 4.5 μm (which is an energy of ~ 0.28 eV) is used.

5.2 Comparison via profile plots

For a profile plot the pixels in a certain region are binned to squares showing the mean value of the binned pixels. With this, one can plot a figure showing the 'profile' of a map, i.e., the abscissa is one space axis of the map and the ordinate shows the mean intensity of the binned pixels. The binning helps to show a larger region and not only a very thin 'pixel row'.
Figure 18 shows a profile plot of the total data map. As expected the intensity is very high along the Galactic plane and becomes less towards higher and lower latitudes, respectively. Interesting is that in the range of the ROI (at $l \approx 30°$ and $b \approx 10°$) the intensity is higher, even if this plot can say nothing about the unexpected excess flux.

[9]http://commander.bitbucket.org/
[10]Detailed descriptions can be found on https://wiki.cosmos.esa.int/planckpla2015/index.php/Astrophysical_component_separation#Commander-Ruler.
[11]Detailed descriptions can be found on https://wiki.cosmos.esa.int/planckpla2015/index.php/CMB_and_astrophysical_component_maps#Astrophysical_foregrounds_from_parametric_component_separation.
[12]http://www.spitzer.caltech.edu/glimpse360/downloads
[13]Some of the Red pixels are filled with value form the *WISE* observation at 12 μm due to the sky coverage from *Spitzer* in this band was less than in the other bands.

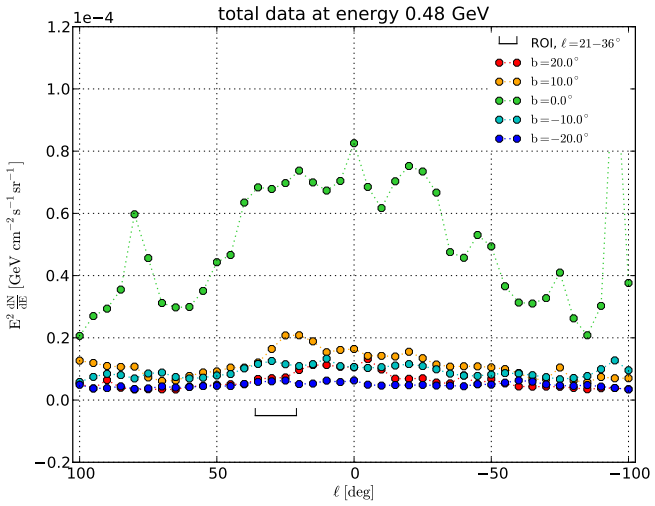

Figure 18: Profile plot of the total data map. The bins of the profile plot have a size of 10° by 10° in Galactic coordinates. The Galactic center is right in the middle of a bin.

5.2.1 Different residual maps

In Figure 19 profile plots for the three residuals in models `A`, `B` and `C` (see section 3.2 for their description) are shown. The residual in model `B` is zero for $\ell > 70°$ to underline that the fit was restricted to the area inside. The values with $\ell < 70°$ have an offset because no isotropic model template was subtracted during calculating the residual map.
On can see that for each map in the range of the ROI an unexpected excess flux is present. This is especially worth mentioning for the residual in model `C`, which was derived by a different method than the other ones.
For this map the calculation of the intensity is more complicated. For the residual in model `C` with its three energy bins it is no calculated exposure map available here. It is replaced by an approximation: assuming the spatial distribution of exposure does not depend on energy, just the exposure used for the total map (see section 3.3) scaled by the fraction of the different observation times is used. For this the resolution of the residual map `C` is degraded (it has a pixelization order of 8, the exposure map just an order of 7), the new pixels with a lower resolution are the mean value of the old pixels[14].

Because the 'bump' also is seen in the residual derived by Acero et al. [Acero et al., 2016] one can state that the unexpected excess in the range of the ROI is a real feature, what shows that it is worth being studied in further investigations.

5.2.2 Maps from other telescopes

Profile plots are also derived from other telescopes' maps. The characteristics of these maps are described above (see section 5.1).

[14]The package 'healpy' that was used here to deal with the via HEALPix stored maps offers a function (`healpy.pixelfunc.ud_grade`) for this.

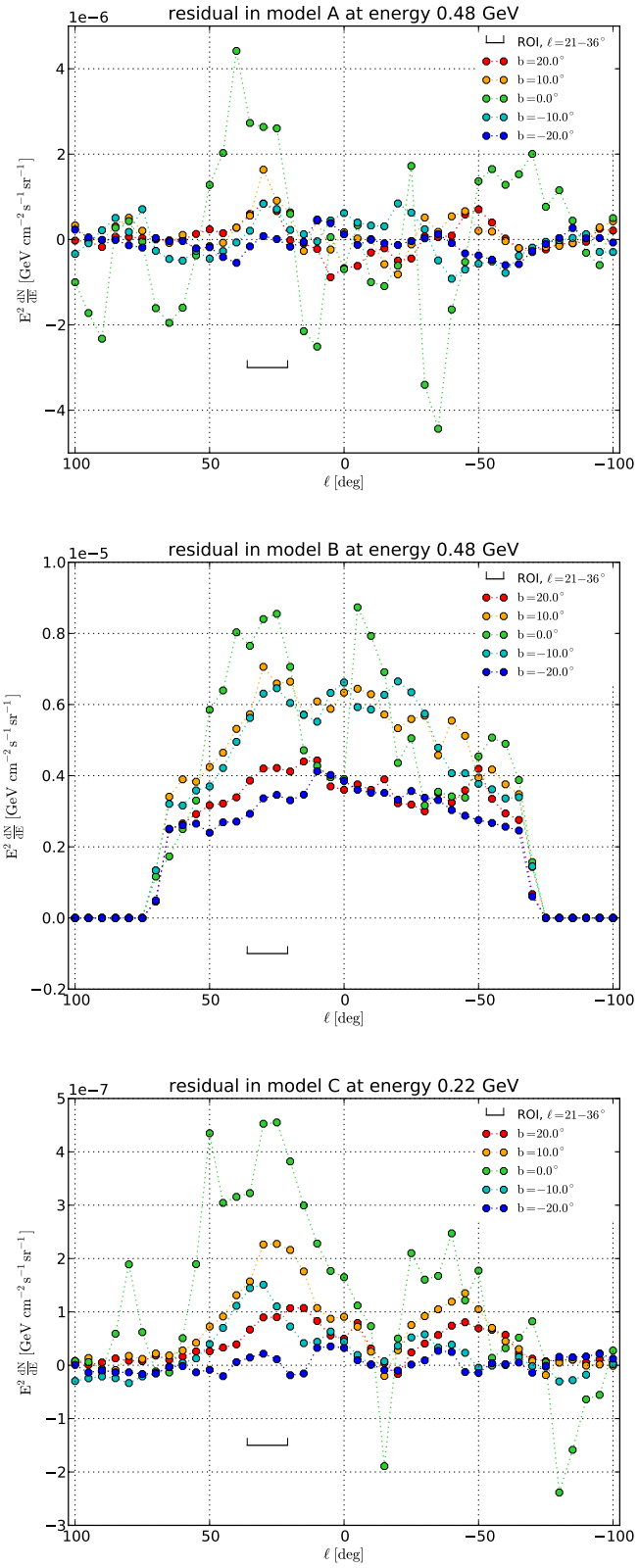

Figure 19: Profile plot of the residual data maps.
Top: Residual in model `A`, *middle:* residual in model `B` and *bottom:* residual in model `C`.
The bins of the profile plot have a size of 10° by 10° in Galactic coordinates. The Galactic center is right in the middle of a bin.

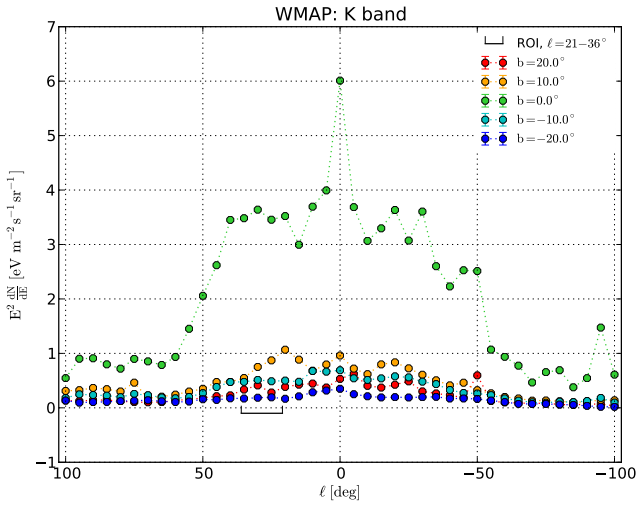

Figure 20: Profile plot of the *WMAP* map at the K band (23 GHz). The bins of the profile plot have a size of 10° by 10° in Galactic coordinates. The Galactic center is right in the middle of a bin.

In Figure 20 one can see the profile of the **WMAP** map at the K band. The correlation between microwave emission and gamma ray emission is mostly via the synchrotron component of the microwave emission. This is caused by the same ultra-relativistic electrons that can up-scatter the interstellar radiation field via IC to gamma energies, this will be discussed in detail below (section 5.3.2).
On can see an excess for middle positive latitudes ($b \approx 10°$), it is approximately symmetric w.r.t. the Galactic center (GC), but it is not w.r.t. the Galctic plane (GP). Microwave radiation can also give a hint on the distribution of dust in the Galaxy. This dust - if hit by CRs - emits also gamma rays due to production and decay of π^0 and bremsstrahlung (see section 2.2.3).
From **Planck** observations Adam et al. [Adam et al., 2015] derived maps showing models for single components. With this a test on a possible correlation of microwave and gamma ray emission separated in processes is possible. In Figure 21 one can see the profile plots for the synchrotron and the thermal dust models derived from *Planck* data with the help of Commander. For the synchrotron model map there is an excess for positive latitudes in the range of the ROI. For middle positive latitudes ($b \approx 10°$) the excess is also approximately symmetric w.r.t. GC, but not w.r.t. GP. For higher positive latitudes ($b \approx 20°$) the excess is not symmetric, neither the GC nor the GP. This seen synchrotron excess is a motivation for further investigations concerning the relation of synchrotron and gamma ray emission in the ROI. A first step for this is done below in section 5.3.2 with *WMAP* data.
At the thermal dust model map also an excess is seen for middle positive latitudes ($b \approx 10°$). It is again approximately symmetric w.r.t. GC, but not w.r.t. GP. Thus also possible correlations of thermal dust and gamma ray emission in the ROI are worth being studied further.
At last also **Spitzer** data is shown. Infrared (IR) is a proxy for star formation because the gas building the stars is heated up during this process and radiating IR light. Star formation is interesting for gamma radiation because regions where stars can be born have a high gas density, this gas can - in combination with CRs - produce gamma rays (π^0 decay and bremsstrahlung).

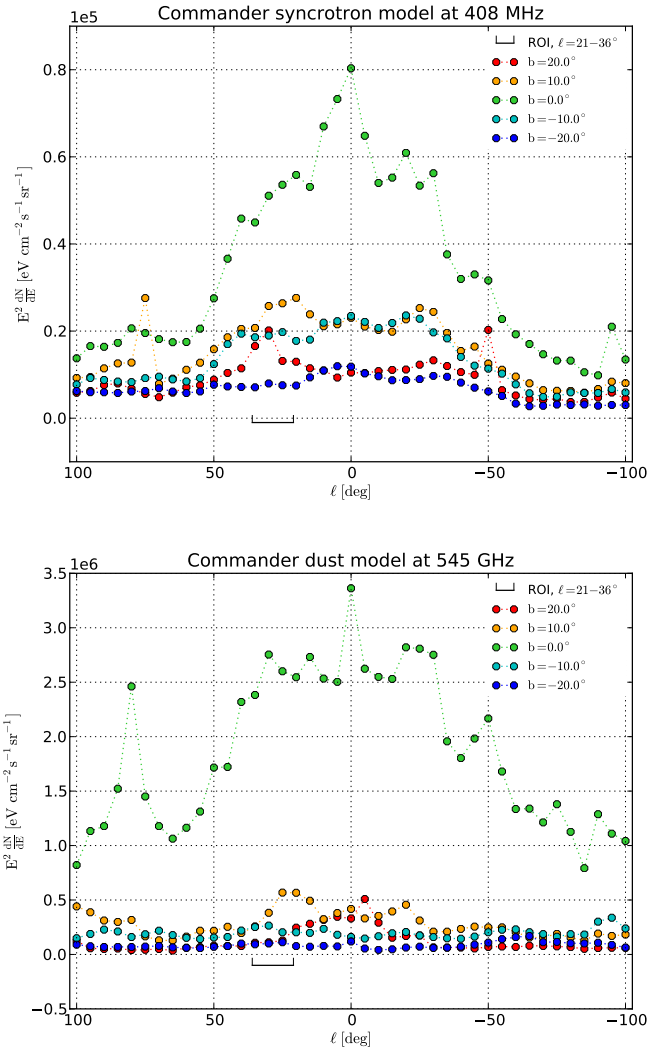

Figure 21: Profile plots of the *Planck* Commander model maps.
Top: Commander syncrotron model map and *bottom:* Commander thermal dust model map.
The bins of the profile plot have a size of 10° by 10° in Galactic coordinates. The Galactic center is right in the middle of a bin.

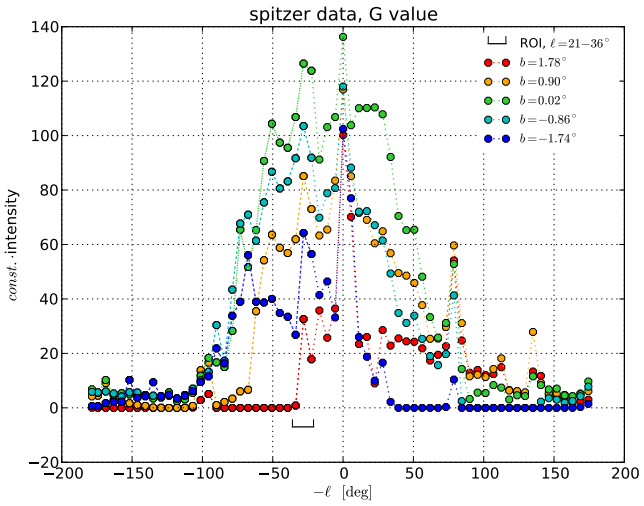

Figure 22: Profile plots of the *Spitzer* map.
The bins of the profile plot have a size of 5.6° by 1.8° in Galactic coordinates. The Galactic center is right in the middle of a bin.

Also the star formation rate is correlated with the rate of supernovae, which are a source of CRs and also gamma rays themselves [Longair, 2011, pp. 361].
In Figure 22 one can see the profile plot of the *Spitzer* map at 4.5 μm. Comparison with the other profile plots should be done carefully because the latitude range covered by this profile is much smaller. Infrared telescopes have a comparatively small field of view, so the *Spitzer* survey mostly mapped the GP and less above and below. Here one can clearly see an excess in the range of the ROI, which is - especially if one is not direct in the GP - not symmetric w.r.t. GC. This excess could be correlated with the gamma ray excess.

In summary, one can say there are a lot of possibilities to further investigate the RIO in different wavelength ranges and to test on correlations between different seen excesses in multiple wavelength ranges and the gamma ray excess.
One of these is started here by analysing if *WMAP* and *Fermi* data components could be effected by the same ultra-relativistic electrons.

5.3 Could *WMAP* and *Fermi* data components be effected by the same electrons?

Ultra-relativistic electrons cause two sorts of radiation: when they travel through a magnetic field they emit synchrotron radiation (see below) and when they travel through a field populated by photons they can up-scatter these to gamma energies due to Inverse Compton effect (IC, see section 2.2.4).

5.3.1 Synchrotron radiation

Synchrotron radiation is interesting here because it has the same source as Inverse Compton radiation since it is also effected by ultra-relativistic electrons. The electrons emit radiation because they are accelerated by a magnetic field B.

For non-relativistic electrons the radiation is called cyclotron radiation, the frequency there is just the frequency of gyration (the circular motion) in the magnetic field B. For ultra-relativistic electrons the emitted frequency spectrum is more complex and can become many times the gyration frequency [Rybicki and Lightman, 2004, p. 167].
Here approximations for the energies of the electrons and - by assuming power law distributions for the electrons and the emitted photons - for the spectral indices are used (see below).

5.3.2 Energy approximation

WMAP is a telescope detecting microwave radiation, see section 5.1. Due to synchrotron radiation also has frequencies in microwave range - among ones in e.g. radio range - it is possible that the same ultra-relativistic electrons cause the microwave photons seen by *WMAP* and the gamma rays seen by *Fermi*. If this is the case, one can correlate the seen effects.
A first approximation of the energy of the electrons radiating synchrotron radiation in the *WMAP* frequencies is the critical frequency ν_c, because most of synchrotron radiation is emitted around this critical frequency [Longair, 2011, eq. 8.55]:

$$\nu_c = \frac{3}{2}\gamma^2 \frac{eB}{2\pi m_e} \sin(\alpha)$$

with γ the gamma-factor and m_e the mass of the electron and B the magnetic field. α is the pitch angle between the magnetic field and the velocity of the electron. In the following α will be set to a maximum pitch angle of 90°.
For example, with a typical magnetic field of $4\,\mu$G the electrons emitting synchrotron radiation with frequencies in the *WMAP* bands have the energies seen in Table 5.

band	K-Band	Ka-Band	Q-Band	V-Band	W-Band
frequency	23 GHz	33 GHz	41 GHz	61 GHz	94 GHz
electron energy	18.9 GeV	22.7 GeV	25.2 GeV	30.8 GeV	38.2 GeV

Table 5: Energies of the electrons emitting synchrotron radiation with frequencies in the *WMAP* bands in a magnetic field of $4\,\mu$G

For the estimation of the photon energy produced in IC a photon from the Cosmic Microwave Background (CMB), the Infrared (IR) and the Starlight (SL) each is up-scattered on the electrons with energies determined above. CMB, IR and SL are chosen because the energy distribution of the Interstellar Radiation Field (ISRF) shows maxima in exactly these frequency ranges (see section 2.2.4). Assuming the electron distribution follows a power law $P(E) \propto E^{-p}$ the energies of the via IC up-scattered photons can be estimated. If $\gamma\hbar\omega_0 \ll m_e c^2$ (γ is the γ-factor of the electron and $\hbar\omega_0$ the energy of the monochromatic photons being up-scattered) is fulfilled, the average energy $\hbar\bar{\omega}$ of the scattered photon is [Longair, 2011, eq. 9.45]:

$$\hbar\bar{\omega} \approx \frac{4}{3}\gamma^2 \hbar\omega_0$$

In Figure 23 the emission spectrum is shown.

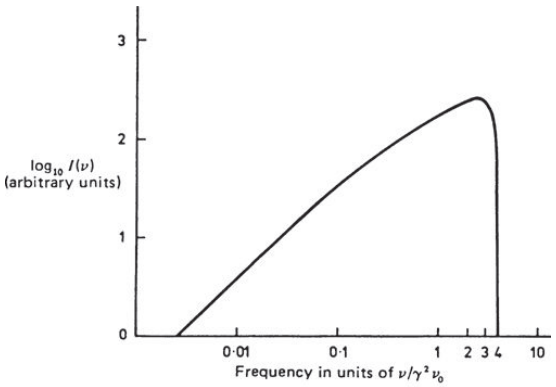

Figure 23: Emission spectrum of Inverse Compton scattering of an incident isotropic photon field at a single frequency off a single electron. ν_0 is the frequency of the un-scattered radiation. The mean value of $\frac{\nu}{\gamma^2 \nu_0}$ lies at $\frac{4}{3}$. [Longair, 2011, p. 242]

Beside the energy the spectral index of the up-scattered photon is of special interest.
First, assuming again a power law distribution for the electron spectrum $P(E) \propto E^{-p}$, its index p can be derived from the index s_{sync} of the radiated synchrotron radiation with the help of the following relation [Rybicki and Lightman, 2004, eq. 6.22b]:

$$s_{sync} = \frac{p-1}{2}$$

Such a relation also exists for the Inverse Compton effect: the spectral index p of power law distributed electrons is related to the index s_{IC} of the via IC up-scattered (assumed as before monochromatic) photons [Rybicki and Lightman, 2004, eq. 7.30]:

$$s_{IC} = \frac{p-1}{2}$$

This is the same relation as for the synchrotron radiation and therefore $s_{sync} = s_{IC}$.

Figure 24 shows the spectrum of the *WMAP* data averaged over the ROI. The calculation of the errors on the spectrum is described in section A.11 (appendix). From this the spectral index can be found through fitting a power law $I = E\frac{dI}{dE} \propto E \cdot E^{s_I}$ to the values. This was done with the help of the same method as described in section 4.2. Below the spectrum the relative difference $\frac{P-I}{I}$ between the fitted power law intensity P and the data intensity I is shown. One finds for the microwave (mw) index $s_{I,\,mw} = 1.065$. The I as an index of the photon spectrum marks it as an index of the intensity flux (and not the photon flux). In Figure 25 one can see the gamma ray spectrum of our ROI. Again the spectrum of the isotropic diffuse gamma ray background [Ackermann et al., 2015b] was subtracted (therefore see also section 4.3). The other data points represent the approximate intensities of the up-scattered CMB, IR and SL. They are made assuming a power law distribution $I = E\frac{dI}{dE} = E \cdot const. E^{-s}$ of the intensity and the (monochromatic) photon frequencies that are shown in Table 6.

The different data points for one ISRF energy correspond to the different *WMAP* bands, the lowest energy corresponds to the lowest band. Because the approximations only give proportionalities the constant *const.* - and therefore the absolute value of the intensity - is an arbitrary

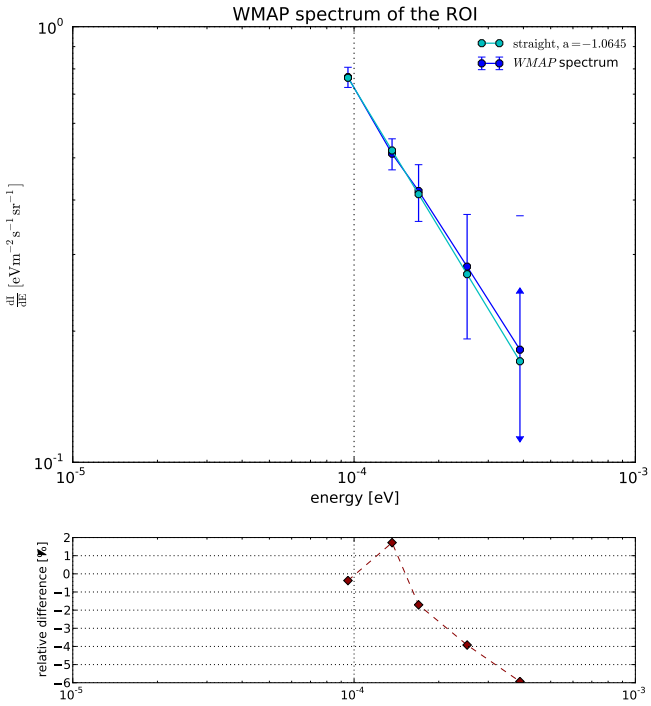

Figure 24: Spectrum of *WMAP* data averaged over the ROI and the fitted power law. It is shown as $\frac{\mathrm{dI}}{\mathrm{dE}}$ over E and both axis are logscale. For the last data point the lower end of the errorbar is negative. Below the relative difference is shown.

ISRF	CMB	IR	SL
frequency	0.24 THz	2.4 THz	240 THz
energy	10^{-3} eV	10^{-2} eV	1 eV

Table 6: Energies of the up-scattered ISRF photons

choice. Here it was chosen to *const.* = $1.45 \cdot 10^{-5}$ in a way that the spectra can be easily compared. Actually the intensities of the three different up-scattered ISRF components are very different. Here for simplicity the constant is assumed to be the same for all components.
The magnetic field has been chosen to a typical value of 4 μG. The energies of up-scattered CMB photons are in a range from ~ 1 MeV to ~ 6 MeV and therefore can not be seen by *Fermi*. The gamma rays caused by IR lie in a range from ~ 10 MeV to ~ 60 MeV and may be seen by *Fermi*, the gamma rays caused by SL appear between ~ 1 GeV to ~ 6 GeV and are surely seen. But as one can see in the Figure 25 the index of the total gamma ray spectrum in the energy range of the up-scattered SL is way harder than the index of the up-scattered SL. The gamma ray index was derived in section 4.2 to a value of $s_{n,\ gamma} = 2.59$. The difference is $s_{n,\ gamma} - s_{I,\ mw} = s_{n,\ gamma} - (s_{n,\ mw} + 1) = 2.59 - 2.06 = 0.53$. Although the shown index of the IC is just an approximation, the difference is rather high.
Therefore the gamma ray spectrum can not be reproduced by SL up-scattered by electrons radiating - due to a 4 μG magnetic field - synchrotron emission seen by *WMAP*.
The up-scattered ISRF components are also plot in a figure with the residual maps, shown in the same way as above. This can be see Figure 26. Here also the index of the up-scattered

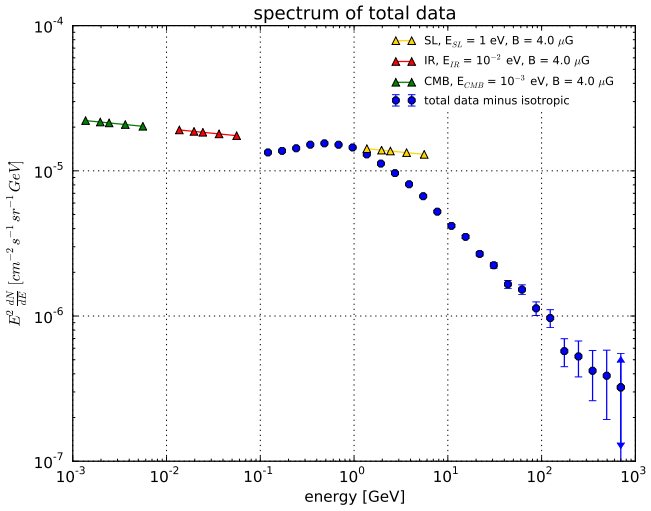

Figure 25: Spectrum of the total data averaged over the ROI and approximate energies of the up-scattered CMB, IR and SL. The magnetic field has a value of B= $4\,\mu$G. From the spectrum of the total data the IGRB spectrum [Ackermann et al., 2015b] was subtracted.
It is shown as $\mathrm{E}^2\frac{\mathrm{dN}}{\mathrm{dE}}$ over E and both axis are logscale. For the last data point the lower end of the errorbar is negative.

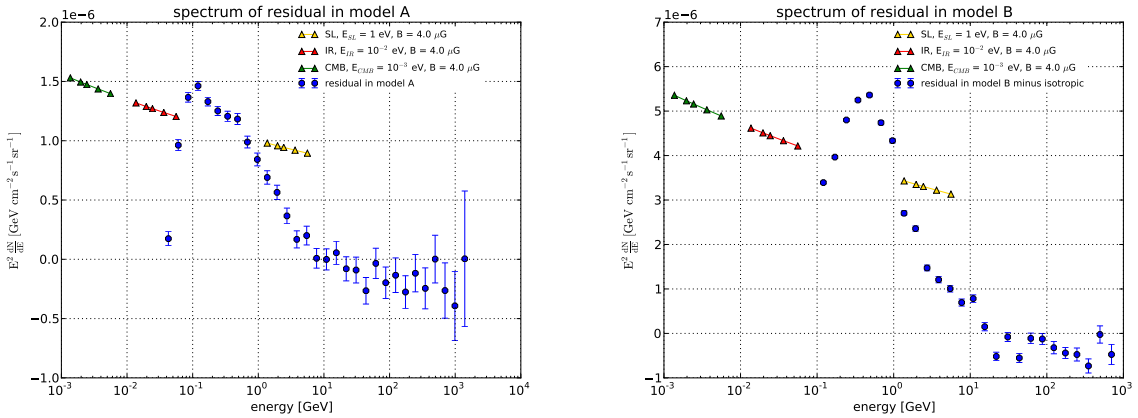

Figure 26: Spectra of the residual data maps averaged over the ROI and approximate energies of the up-scattered CMB, IR and SL. The magnetic field has a value of B= $4\,\mu$G.
Left: residual in model `A`, *right:* residual in model `B` minus the isotropic spectrum.
It is shown as $\mathrm{E}^2\frac{\mathrm{dN}}{\mathrm{dE}}$ over E and only the energy axis is logscale.

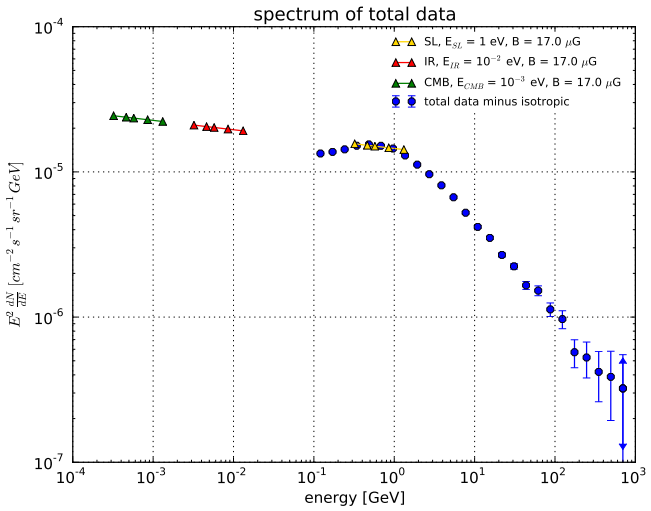

Figure 27: Spectrum of the total data averaged over the ROI and approximate energies of the upscattered CMB, IR and SL with increased magnetic field. B now has a value of 17 μG. From the spectrum of the total data the isotropic spectrum was subtracted. It is shown as $E^2 \frac{dN}{dE}$ over E and both axis are logscale. For the last data point the lower end of the errorbar is negative.

SL can not reproduce the indices of the residual maps. With this one can conclude that SL up-scattered by electrons radiating - due to a 4 μG magnetic field - synchrotron emission seen by *WMAP* also can not explain the seen residual.

Because of the magnetic field being set to some assumed value, the energy range of the up-scattered photons can be adjusted by assuming another value for it and with this - because we have a fixed synchrotron frequency - assuming another electron energy. The index can not be adjusted because it depends only on the measured *WMAP* spectral index.
So changing the magnetic field until the IC photons from SL contribute at the maximum, where the index of the RIO spectrum is way softer, results in a relatively high value of $B \approx 17\,\mu$G. The value was chosen via a fit by eye and the result can be seen in Figure 27.
The magnetic field of $B = 17\,\mu$G (with fixed frequency of the emitted synchrotron radiation) lead to the in Table 7 shown electron energies we are looking at.

band	K-Band	Ka-Band	Q-Band	V-Band	W-Band
electron energy	9.17 GeV	11.0 GeV	12.2 GeV	14.9 GeV	18.5 GeV

Table 7: Energies of the electrons emitting synchrotron radiation with frequencies in the *WMAP* bands in a magnetic field of 17 μG

The choice for the SL to contribute at the maximum of the gamma ray spectrum was made because the intensity of the ISRF in SL wavelength is by a factor of around five larger than the intensity in IR frequencies (see also section 2.2.4). This magnetic field implies that the energy of up-scattered IR is in a range of ~ 2 MeV to ~ 20 MeV and therefore can not be seen by *Fermi*. Up-scattered CMB still does not contribute to gamma rays seen by *Fermi* at all.

For the ROI this implicates:
- either there is no strong correlation between the excess seen at *WMAP* data and the one seen by *Fermi* and therefore the gamma ray excess flux in the ROI has a rather low distribution from IC emission which is produced by electrons their synchrotron radiation is seen by *WMAP*
- or the following conditions are (in some relation) fulfilled:
an area in the line of sight at 30° longitude is populated by some ultra-relativistic electrons with energies around $\sim 10\,\mathrm{GeV}$ which emit - due to a relatively high magnetic field of $\sim 17\,\mu\mathrm{G}$ - synchrotron radiation in *WMAP* frequencies. They cause the excess with the seen spectrum in microwave frequencies and also up-scatter SL to gamma energies seen by *Fermi*.

This analysis here does not yet answer this question finally. Basing on the acquired knowledge both options can be considered possible. The question for further investigations is which (or which combination) is preferred.

6 Outlook

In this work the excess flux at 30° longitude is investigated in different ways.

- The spectra of the total data and the residual data averaged over the ROI are derived and compared with all-sky spectra. Both (or better all three) could not be explained by a linear combination of the whole sky emission process spectra. This leads to the conclusion that something new and yet unexplored is going on there.
- Multiwavelength analysis showed that in this region excesses also are seen in other wavelength ranges. This leads to multiple possibilities for further studies whether these are correlated with the gamma ray excess or not.
- A first step in this regard was the question, if *WMAP* and *Fermi* data in this region could be effected by the same ultra-relativistic electron population. The question is not yet answered finally, but with the rather high magnetic field of $\geq 15\,\mu$G a requirement for a correlation was found.

In future tests, e.g., the following improvements could be included:

- One could determine the boundaries of the ROI by some calculations and not by eye, e.g., select it from the residual maps by choosing a threshold for the derivative from the model.
- One could model the different emission components with varying assumptions and particular observance of the ROI.
- One could continue the multiwavelength analysis by testing for correlations between the seen excesses and the gamma excess.

...and of course many other things.

Overall the existence of the excess at 30 degrees in longitude in the plane of the Milky Way galaxy is confirmed and a lot of possibilities for further investigations of the excess are found.

A Appendix

A.1 GALPROP parameters for model `A`

CR diffusion with	Kolmogorov spectrum of interstellar turbulence plus reacceleration no convection
diffusion coefficient	constant and isotropic
azimurthal symmetry of the CR density	assumed w.r.t. GC
CR source distribution	traced by measured pulsar distribution
CR confinement volume	10 kpc height 20 kpc radius

Table 8: Parameters for GALPROP used to generate model `A`

A.2 Borders of the interstellar gas annuli assumed for model `A`

annulus	inner radius	outer radius	
1	0 kpc	1.5 kpc	inner ring
2	1.5 kpc	3.5 kpc	inner ring
3	3.5 kpc	8 kpc	inner ring
4	8 kpc	10 kpc	local ring
5	10 kpc	50 kpc	outer ring

Table 9: Galactocentric radii of the interstellar gas annuli assumed to generate model `A`. The distance from the Galactic center to the sun is ~ 8.3 kpc [Gillessen et al., 2009].

A.3 Parameters for the shells modelling Loop I for model `A`

shell	longitude coordinate	latitude coordinate	distance to the center	inner radius	outer radius
1	341°	3°	78 pc	62 pc	81 pc
2	332°	37°	95 pc	58 pc	82 pc

Table 10: Parameters for the shells modelling Loop I to generate model `A`

A.4 Figures showing the hadronic, IC and Loop I templates for model A

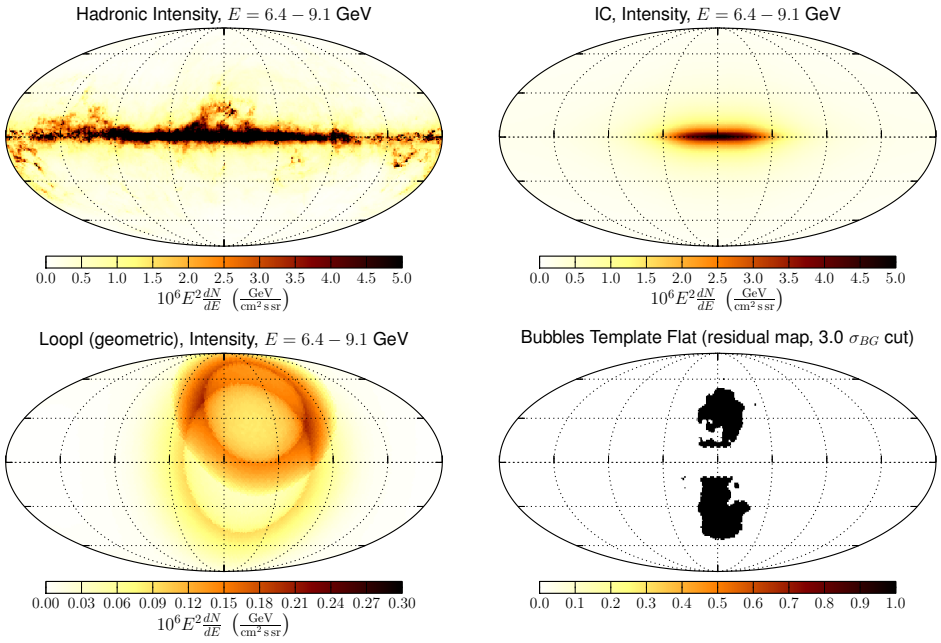

Figure 28: Hadronic, IC, Loop I and *Fermi* bubbles templates for model A. The template intensities are shown in the energy bin $E = 6.4 - 9.1$ GeV. *top left:* gas correlated template (sum of hadronic and bremsstrahlung for neutral and ionized atomic and molecular hydrogen) obtained from GALPROP. *top right:* IC map obtained from GALPROP. *bottom left:* Loop I template based on geometrical model [Wolleben, 2007]. The normalization is obtained by fitting to the *Fermi* LAT data. *bottom right:* Flat *Fermi* bubbles template. [Ackermann et al., 2014, Figure 2 and 5 there]

A.5 Characteristics of the map used to generate model C

class	P7REP Clean
observation time	first 4 years of the mission
zenith angle cut	$\theta < 100°$
energy bins	14 equal logarithmic intervals
energy range	50 MeV - 50 GeV
HEALPix[15] pixelization order	8
HEALPix nside value	256
pixel size	$1.6{\cdot}10^{-5}$ sr

Table 11: Characteristics of the data sample used to generate residual map C

[15] http://sourceforge.net/projects/healpix/

A.6 Calculation of the standard derivation on the mean intensity

The standard derivation on the mean intensity is calculated from the counts assuming a Poisson statistics for the counts. Random events occur in a Poisson distribution when for one event the possibility to occur in one moment is not correlated with the time passed since the former event. For a Poisson distribution the relative error (standard derivative) σ_{rel} for a certain number of events in a bin - here for a photon count value in a certain pixel - is given by:

$$\sigma_{rel,i} = \frac{1}{\sqrt{counts_i}}$$

where $counts_i$ is the number of counts in the pixel i. The absolute error is $\sigma_{abs,i} = \sigma_{rel,i} \cdot counts_i = \sqrt{counts_i}$.

For a quantity $x = c_1\ a + c_2\ b$, where a and b are independent random variables and c_1, c_2 constants, the absolute error is:

$$\sigma_x^2 = \left(\frac{\partial x}{\partial a}\right)^2 \sigma_a^2 + \left(\frac{\partial x}{\partial b}\right)^2 \sigma_b^2 = c_1^2\ \sigma_a^2 + c_2^2\ \sigma_b^2$$

The error on the mean counts $x = \langle counts \rangle_i = \frac{1}{n_{pix}} \sum_i counts_i = \sum_i \frac{1}{n_{pix}} a_i$ is with this (the error on the exposure is assumed to be zero):

$$\sigma_{abs,\ mean} = \sqrt{\sum_i \frac{1}{n_{pix}}^2 \sigma_{abs,\ i}^2} = \frac{1}{n_{pix}} \sqrt{\sum_i \left(\sqrt{counts_i}\right)^2} = \frac{1}{n_{pix}} \sqrt{\sum_i counts_i}$$

and

$$\sigma_{rel,\ mean} = \frac{\sigma_{abs,\ mean}}{\langle counts \rangle_i} = \frac{\frac{1}{n_{pix}} \sqrt{\sum_i counts_i}}{\frac{1}{n_{pix}} \sum_i counts_i} = \frac{1}{\sqrt{\sum_i counts_i}}$$

With this the absolute error on the intensity is (ΔE does not name an error on the energy but the width of the energy bin):

$$\Delta I = \Delta\left(E^2\ \frac{counts}{exposure\ \Delta E\, \mathrm{d}\Omega}\right) = E^2\ \frac{\Delta counts}{exposure\ \Delta E\, \mathrm{d}\Omega} = E^2\ \frac{\sigma_{abs}}{exposure\ \Delta E\, \mathrm{d}\Omega} = \sigma_{rel} \cdot I$$

And on the mean intensity:

$$\begin{aligned}\Delta \langle I \rangle_{ROI} &= \Delta\left(E^2\ \langle \frac{counts}{exposure} \rangle_{ROI} \frac{1}{\Delta E\, \mathrm{d}\Omega}\right) = \frac{E^2}{\Delta E\, \mathrm{d}\Omega} \frac{1}{n_{pix}} \sqrt{\sum_i \frac{\sigma_{abs,\ mean}^2}{exposure_i^2}} \\ &= \frac{E^2}{\Delta E\, \mathrm{d}\Omega} \frac{1}{n_{pix}} \sqrt{\sum_i \frac{counts_i}{exposure_i^2}}\end{aligned}$$

Here now one hast to assumed that the spatial distribution of the exposure is small and therefore the difference between the pixels in the restricted ROI can be neglected for the exposure. With

this:

$$\begin{aligned}\Delta\langle I\rangle_{ROI} =& \frac{E^2}{\Delta E\,\mathrm{d}\Omega}\frac{1}{n_{pix}\ exposure}\sqrt{\sum_i counts_i} = \frac{E^2}{\Delta E\,\mathrm{d}\Omega}\frac{1}{n_{pix}\ exposure}\frac{\sum_i counts_i}{\sqrt{\sum_j counts_j}} \\ =& \frac{E^2}{\Delta E\,\mathrm{d}\Omega}\frac{1}{n_{pix}}\sum_i \frac{counts_i}{exposure_i\sqrt{\sum_j counts_j}} = \frac{1}{\sqrt{\sum_j counts_j}}\frac{E^2}{\Delta E\,\mathrm{d}\Omega}\frac{1}{n_{pix}}\sum_i \frac{counts_i}{exposure_i} \\ =& \sigma_{rel,\ mean}\cdot\langle I\rangle_{ROI}\end{aligned}$$

For the residual maps the (mean) intensity is derived the same way as for the total data map. Here now $x = residual = data - model = a + b$. Because the models are fit as all-sky templates and we derive our data and residual intensities in a small ROI, $\sigma_b = \sigma_{model}$ can be neglected (especially in each pixel). So the absolute error on the residual data maps results to be:

$$\sigma_{abs,\ res} = \sigma_a + 0 = \sigma_{abs}$$

And therefore it is the same as for the total counts. With this the mean error is also the same:

$$\sigma_{abs,\ res,\ mean} = \frac{1}{n_{pix}}\sqrt{\sum_i counts_i}$$

And also the absolute error on the mean intensity $\Delta\langle I_{res}\rangle_{ROI}$ is the same:

$$\begin{aligned}\Delta\langle I_{res}\rangle_{ROI} =& \Delta\Big(E^2\ \langle\frac{residual\ counts}{exposure}\rangle_{ROI}\frac{1}{\Delta E\,\mathrm{d}\Omega}\Big) = \frac{E^2}{\Delta E\,\mathrm{d}\Omega}\frac{1}{n_{pix}}\sqrt{\sum_i \frac{\sigma^2_{abs,\ res,\ mean}}{exposure_i^2}} \\ =& \frac{E^2}{\Delta E\,\mathrm{d}\Omega}\frac{1}{n_{pix}}\sqrt{\sum_i \frac{\sigma^2_{abs,\ mean}}{exposure_i^2}} = \sigma_{rel,\ mean}\cdot\langle I\rangle_{ROI} = \Delta\langle I\rangle_{ROI}\end{aligned}$$

A.7 Spectrum of the total data and fitted power law

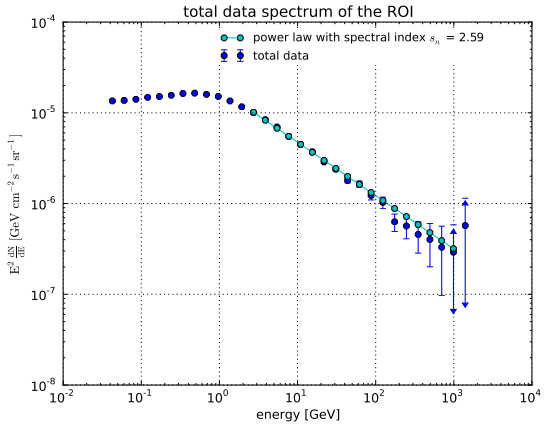

Figure 29: Spectrum of the total data and fitted power law $I = const.\ E^{-s_n+2}$.
It is shown as $\mathrm{E}^2\frac{\mathrm{dN}}{\mathrm{dE}}$ over E and both axis are logscale. For the last two datapoints the lower end of the errorbar is negative.

A.8 Characteristics of the map used for the IGRB analysis

class	modified P7 UltraClean class, parted in two energy ranges (even harder cuts were made, different for low energies and high energies)
observation time	50 month recorded between August 5, 2008 and October 6, 2012
energy bins	26 equal logarithmic intervals
energy range	'low energies': 100 MeV - 13 GeV 'high energies': 13 GeV - 820 GeV
zenith angle cut	for low energies $\theta < 90°$ for high energies $\theta < 105°$

Table 12: Characteristics of the data sample used to generate the IGRB spectrum

A.9 Mask used during the fit for the IGRB analysis

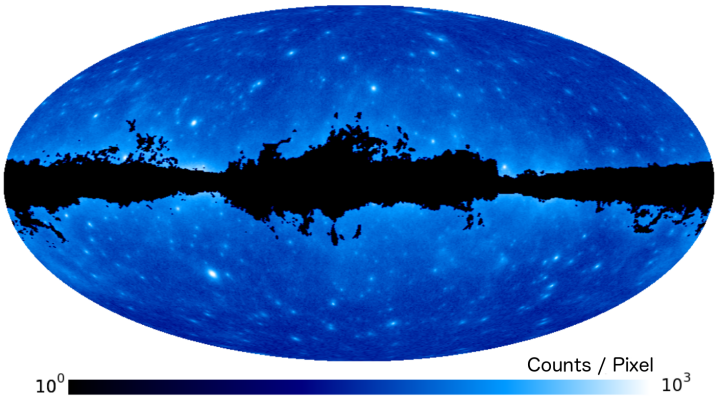

Figure 30: Map of counts observed by the *Fermi* LAT above 100 MeV using a Mollweide projection. The color scale is logarithmic. Overlaid is the mask used in their analysis to exclude regions from the template fitting procedure [Ackermann et al., 2015b, Figure 3 there].

A.10 Spectrum of the model μ and fitted power law

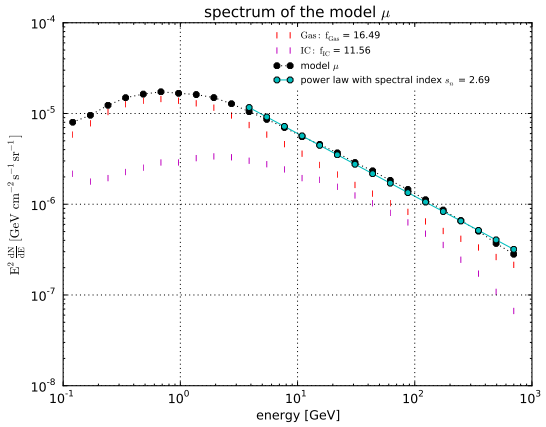

Figure 31: Spectrum of the model μ and fitted power law $I = const.\ E^{-s_n+2}$. The errors on the model values are set the same for each data point.
It is shown as $\mathrm{E}^2 \frac{\mathrm{dN}}{\mathrm{dE}}$ over E and both axis are logscale.

A.11 Calculation of the errors on the *WMAP* spectrum

In section 5.3.2 the spectrum of *WMAP* data averaged over the ROI is derived. The maps are given in a brightness temperature T_b, the corresponding intensity is calculated via the Rayleigh-Jeans approximation. The errors σ_i on the intensity values in every pixel i are encoded in the maps as follows (here all σ are total standard derivations):

$$\sigma_i^2 = \frac{\sigma_0^2}{N_{obs,\ i}}$$

The number of observations N_{obs} is also a map and part of the *WMAP* data file, $N_{obs,\ i}$ is its value in the i-th pixel.
σ_0 is the radiometer noise for an individual sample and a constant only depending on the energy band. Its value is taken from Bennett et al. [Bennett et al., 2013, Table 5 there] and here shown in Table 13. For the higher bands there is more than one radiometer per band and therefore there are more σ_0 values, for this analysis the mean is taken.

	K-Band	Ka-Band	Q-Band (1)	Q-Band (2)	V-Band (1)	V-Band (2)
σ_0	1.429	1.466	2.245	2.131	3.314	2.949

	W-Band (1)	W-Band (2)	W-Band (3)	W-Band (4)
σ_0	5.899	6.562	6.941	6.773

Table 13: σ_0 values of the different *WMAP* bands

Now for the mean intensity the standard derivative is calculated as follows:

$$\sigma_{mean}^2 = \sum_i \frac{1}{n_{pix}^2}\sigma_i^2 = \frac{\sigma_0^2}{n_{pix}^2}\sum_i \frac{1}{N_{obs,\ i}}$$

$$\Rightarrow \sigma_{mean} = \frac{\sigma_0}{n_{pix}}\sqrt{\sum_i \frac{1}{N_{obs,\ i}}}$$

List of Figures

References

[Abergel et al., 2014] Abergel, A. et al. (2014). Planck 2013 results. XI. All-sky model of thermal dust emission. *Astronomy & Astrophysics*, 571. arXiv:1312.1300.

[Acero et al., 2015] Acero, F. et al. (2015). Fermi Large Area Telescope Third Source Catalog. *Astrophysical Journal Supplement Series*. arXiv:1501.02003.

[Acero et al., 2016] Acero, F. et al. (2016). Development of the Model of Galactic Interstellar Emission for Standard Point-Source Analysis of Fermi Large Area Telescope Data. *The Astrophysical Journal*, 223(26). arXiv:1602.07246.

[Ackermann et al., 2014] Ackermann, M. et al. (2014). The Spectrum and Morphology of the Fermi Bubbles. *The Astrophysical Journal*, 493(64). arXiv:1407.7905.

[Ackermann et al., 2015a] Ackermann, M. et al. (2015a). Deep view of the Large Magellanic Cloud with six years of Fermi -LAT observations. *Astronomy & Astrophysics*. arXiv:1509.06903.

[Ackermann et al., 2015b] Ackermann, M. et al. (2015b). The spectrum of isotropic diffuse gamma-ray emission between 100 MeV and 820 GeV. *The Astrophysical Journal*, 799(86). arXiv:1410.3696.

[Adam et al., 2015] Adam, R. et al. (2015). Planck 2015 results. X. Diffuse component separation: Foreground maps. *Astronomy & Astrophysics*. arXiv:1502.01588.

[Bennett et al., 2013] Bennett, C. L. et al. (2013). Nine-Year Wilkinson Microwave Anisotropy Probe (WMAP) Observations: Final Maps and Results. *Astrophysical Journal Supplement Series*. arXiv:1212.5225.

[Dame et al., 2001] Dame, T. M. et al. (2001). Milky Way in Molecular Clouds: A New Complete CO Survey. *The Astrophysical Journal*, 547(792). http://adsabs.harvard.edu/abs/2001ApJ...547..792D.

[Gillessen et al., 2009] Gillessen, S. et al. (2009). Monitoring Stellar Orbits around the massive Black Hole in the Galctic Center. *The Astrophysical Journal*, 692.

[Haslam et al., 1982] Haslam, C. G. T. et al. (1982). A 408 MHz all-sky continuum survey. II - The atlas of contour maps. *Astronomy and Astrophysics Supplement Series*. http://adsabs.harvard.edu/abs/1982A

[Herbst, 1995] Herbst, E. (1995). Chemistry in the Interstellar Medium. *Annu. Rev. Phys. Chem.*, 46:27–53.

[Kalberla et al., 2005] Kalberla, P. et al. (2005). The Leiden/Argentine/Bonn (LAB) Survey of Galactic HI. Final data release of the combined LDS and IAR surveys with improved stray-radiation corrections. *Astronomy & Astrophysics*, 440(775). http://adsabs.harvard.edu/abs/2005A

[Kataoka et al., 2013] Kataoka, J. et al. (2013). Suzaku observations of the diffuse x-ray emission across the fermi bubbles' edges. *The Astrophysical Journal*, 779(57). arXiv:1310:3553.

[Longair, 2011] Longair, M. S. (2011). *High Energy Astrophysics*. Cambridge University Press, Cambridge, 3 edition.

[NASA, 2011] NASA (2011). Description of the Large Area Telescope (LAT). http://fermi.gsfc.nasa.gov/science/instruments/lat.html and http://fermi.gsfc.nasa.gov/science/instruments/table1-1.html.

[Preibisch and Mamajek, 2008] Preibisch, T. and Mamajek, E. (2008). *Handbook of Star Forming Regions: Volume II, Chapter 2: The Nearest OB Association: Scorpius-Centaurus (Sco OB2)*. Astronomical Society of the Pacific. arXiv:0809.0407.

[Rybicki and Lightman, 2004] Rybicki, G. B. and Lightman, A. P. (2004). *Radiative Processes in Astrophysics*. John Wiley & Sons, New York.

[Schlegel et al., 1998] Schlegel, D. J. et al. (1998). Maps of Dust Infrared Emission for Use in Estimation of Reddening and Cosmic Microwave Background Radiation Foregrounds. *The Astrophysical Journal*, 500(2). http://adsabs.harvard.edu/abs/1998ApJ...500..525S.

[Strong et al., 2004] Strong, A. W. et al. (2004). Diffuse Galactic continuum gamma rays. A model compatible with EGRET data and cosmic-ray measurements. *The Astrophysical Journal*, 613:962–976. arXiv:astro-ph/0406254.

[Tibaldo and Grenier, 2013] Tibaldo, L. and Grenier, I. (2013). The Fermi LAT view of Cygnus: a laboratory to understand cosmic-ray acceleration and transport. *Nuclear Physics B*. arXiv:1211.3165.

[Wolleben, 2007] Wolleben, M. (2007). A New Model For The Loop-I (The North Polar Spur) Region. *The Astrophysical Journal*, 664:349–356. arXiv:0704.0276.

Acknowledgements

Here I want to thank all the people, that helped me for this theses.

- First of all Prof. Dr. Stefan Funk for offering the topic to me, it was very exiting and interesting. I really have learned a lot during writing this thesis.
- Also I want to thank Prof. Dr. Gisela Anton for carrying out the 'Zweitgutachten'.
- Moreover Dmitry Malyshev for looking after me during my work. It has been a pleasure to work with you.
- All the people in the gamma group, for the friendly accommodation and inclusion.
- Felix Schleifer, Jackeline Catalano, Berhard Akstaller and Laura Herold for the proofreading and for finding a lot mistakes.
- And all my friends and my family for their tireless encouragement and support and because they are just really cool.

Thank you very much! :)

Eidesstattliche Erklärung

Ich versichere hiermit an Eides statt, dass ich die vorliegende Bachelorarbeit mit dem Titel "Analysis of an excess flux of gamma rays at 30 degrees in longitude in the plane of the Milky Way galaxy" selbstständig und ohne unzulässige fremde Hilfe erbracht habe. Ich habe keine anderen als die angegebenen Quellen und Hilfsmittel benutzt sowie wörtliche und sinngemäße Zitate kenntlich gemacht. Die Arbeit hat in gleicher oder ähnlicher Form noch keiner Prüfungsbehörde vorgelegen.

Ort, Datum

Unterschrift

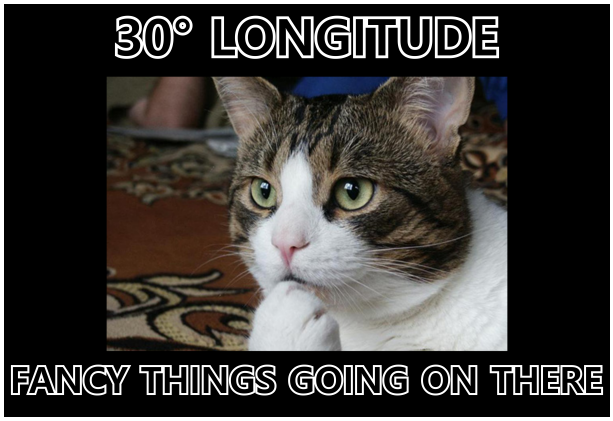
30° LONGITUDE
FANCY THINGS GOING ON THERE